Investigating pyrite genesis and relation to gold at the Lone Star Deposit, YT

By

Arthur E. Hilliard

Submitted in partial fulfillment of the requirements for the degree of Bachelor of Science in Earth Science

at

Dalhousie University

Halifax, Nova Scotia

April 2023

Supervisor: Dr. James Brenan

TABLE OF CONTENTS

LIST OF FIGURES

LIST OF TABLES

Abstract

The Klondike region of the Yukon Territory, Canada, is famous for extensive placer deposits, recovering over 20 million oz since discovery, but lacks any major defined bedrock resources. As a result of a surge in exploration activity, recent drilling efforts have delineated several new bedrock targets, including the Lone Star deposit near Dawson City, Yukon. The Lone Star deposit is hosted by a suite of Late Permian plutonic, volcanic, and sedimentary units known as the Klondike Assemblage. This assemblage formed because of subduction-related arc-magmatism, followed by Late Permian-Early Triassic regional greenschist-amphibolite facies metamorphism during accretion onto Laurentia as part of the Yukon-Tanana Terrane. Gold deposition is thought to be mid-late Jurassic, mainly occurring within discordant quartz veins with common pyrite mineralization but overall low sulfidation (galena, sphalerite, chalcopyrite, etc. only trace). This study adds to the overall understanding of the Lone Star deposit by establishing relations between pyrite paragenesis and gold mineralization. This is done through detailed examination of a suite of samples, selected based on differences in pyrite occurrence. Observations by reflected light and SEM have delineated at least 3 major pyrite types from a textural perspective: syn-tectonic, post-tectonic and vein. Samples have been analyzed by LA-ICPMS using individual spot analyses on pyrite core and rim, and trace element mapping on a subset of samples. Of the trace element suite measured, we found consistently detectable levels of Co, Ni, Cu, As, Sb, Pb, Te and Bi. Spot analyses have revealed both discrete core-rim trace element concentrations and grains that are relatively homogeneous, providing evidence for pyrite growth events involving different trace element sources. Trace element maps reveal these relations in more detail with grains displaying internal chemical structure. Some elements (Co, Ni, As, in some cases Se) are present as a dissolved component, but others (Cu, Sb, Pb, Te, and Bi) are typically found as inclusions along with Au and Ag in small amounts. Cores tend to be enriched in Co, Ni, or As, with rims depleted relatively. Gold concentrations are below detection in pyrite grains and is present as sparse inclusions of an Au or Au-Te phase. The occurrence of Au as a discrete phase, and not a dissolved component, suggest that a disconnect exists between the processes that precipitated gold and those that formed pyrite in the Lone Star system.

Keywords: orogenic gold, pyrite, trace elements, LA-ICPMS mapping

Acknowledgements:

Many people came together to help me make this project happen, and I won't be able to cover them all in this section. A big thanks to my advisor, James Brenan for guiding me through this study, and the members of his research group, Kathleen Clark and Peteris Rozenbaks, who helped me with sample preparation and LA-ICPMS setup. I also owe my gratitude to the awesome crew I had the pleasure of working alongside with in the field last summer, which included PhD student Nelson Roman and his advisor Dan Gregory from the University of Toronto who helped me get a start on my thesis and provided assistance along the way.

Introduction

1.1 Deposit background

Situated at the confluence of Eldorado and Bonanza creek in the Klondike region of the Yukon Territory, the Lone Star deposit has long been a prospective site for lode gold in the area (MINFILE 115O 180; McConnell, 1905). This region has historical significance for being host to the last great North American gold rush in 1896, driven by extensive placer discoveries on both the Eldorado and Bonanza creeks. Still today, new mining operations are developed regularly along these streams, but mechanisms of lode sources remain debated. Original reports dating back to the early 20th century identified gold linked to discordant quartz veins (McConnell, 1905), and it is clear from more modern work (Knight et al 1999, Chapman et al., 2010) that there is a strong chemical link between economic placer deposits and local lode discoveries, making the Lone Star region one of particular interest. Like many deposits, gold is found associated with pyrite in field relationships, and work has documented the occurrence of native Au in microfractures cross cutting earlier vein generations as well as pyrite grains (Grimshaw, 2018). By investigating pyrite chemistry, one can interpret whether gold was sourced directly from pyrite grains internally or from a distal source, while providing an opportunity to examine the processes responsible for ore mineral formation in this deposit. In this study, this was accomplished by applying LAICP-MS imaging and spot analysis techniques in combination with textural and mineralogical correlations, determining discrete pyrite generations and the chemical associations within them.

1.2 Regional geology

The Lone Star deposit is in the allochthonous Yukon-Tanana Terrane (YTT) (Fig 1), within the broadly compressional tectonic regime of the Northwestern-Cordillera, which initiated following subduction along the Laurentian craton in the Late-Devonian (Dickenson, 2004; Nelson & Colpron, 2007). This is roughly synchronous with the deposition of the underlying units to our study area, the peri-cratonic Snowcap assemblage (Piercy & Colpron, 2009). Shortly after westward subduction began in the late-Devonian to early-Mississippian, likely because of slab rollback (Piercy et al, 2004), there was a shift to eastward subduction, which opened the

Slide Mountain Ocean and separated the early YTT from Laurentia (Nelson et al., 2006). The units we are interested in are hosted within the Klondike assemblage, which formed as a volcanic arc sequence in the brief period when subduction was switching back to the West to consume the Slide Mountain Ocean in the Late-Permian (Nelson et al., 2006). This event culminated in the Klondike Orogeny (Beranek & Mortenson, 2011), resulting in regional greenschist-amphibolite facies metamorphism and, over its evolution, generation of an S1 fabric followed by recrystallization into a pervasive S2 foliation fabric, finally being variably overprinted by S3 crenulations (Mackenzie et al., 2008). In many samples, these crenulations can make the fabric of the matrix difficult to decipher, but it is clear in some places and can be described as a spaced crenulation cleavage (Grimshaw, 2018). Because of continued thrust stacking of outboard terranes (Mackenzie et al., 2007a), the region was exposed to protracted metamorphic conditions and overprinted by D4 events in the Jurassic, the latter of which is often host to gold-bearing quartz veins and possibly produced sulfides (Mackenzie et al., 2008). Regionally, extensional D5 faulting was occurring by the Cretaceous, and is associated with sulfidation in some silicified schist sections (Mackenzie et al., 2008). These observations are consistent with work describing mineralization as post-orogenic (Allan et al., 2014), and devolatization reactions associated with ongoing metamorphism have been speculated as a source for Au-bearing fluids originating at depth (Grimshaw, 2018). Many gold deposits in regions like this are formed across the greenschist-amphibolite facies (Tomkins, 2010) and in general, regional structure characteristics and gold occurrence follow those originally outlined for orogenic gold deposits by Groves et al. (1998).

1.3 Local geology

Historically, work in this region has struggled with accurate geologic classifications, likely due to extensive weathering as well as progressive recrystallization events making lithologies cryptic to decipher. Field relations group the main expressions of the Klondike assemblage at Lone Star into two categories: felsic and intermediate schist, (Jutras & Kenwood, 2022) shown in a regional geology map in Figure 2. Mortenson et al. (2019) provides unit descriptions that differentiate our units somewhat, and observations of mineralogy generally reflect some of these classifications. The first unit of interest is classified as a muscovite quartzite (MQ), which makes up the felsic schist member (Mortenson et al., 2019) and is the most distinctive in the field, with

generally low sulphide and gold content, a comparatively siliceous composition, and a more competent, blocky weathering habit. The fabric of this unit is usually dominated by S2 and generally lacks structures hosting quartz veins. Next, part of the intermediate member, there is a quartz-muscovite schist (QMS) that is described as relatively pyritic and plays host to both disseminated gold and gold-bearing quartz veins (Mortenson et al., 2019). Field observations of fabric in this unit are variable; it has been recrystallized by S2 but is variably overprinted by S3 as well as D4 fold and kink structures, variably hosting quartz veins. Also included in the intermediate member is a quartz-chlorite-muscovite schist (QCMS), described as non-pyritic (Mortenson et al., 2019). Bulk compositions plot in dacite (QMS and QCMS) and rhyolite (MQ) fields on total-alkali silica and Zr/Ti vs Nb/Y diagrams (Mortenson et al., 2019), implying overall felsic bulk compositions (Fig 3). QCMS and QMS differentiations do not correlate perfectly with descriptions observed in the field and in our samples, mainly regarding chlorite and pyrite contents. For this study, these will be considered together as QMS under the intermediate schist classification, because, in practice, described units exist on some sort of lithologic and metamorphic continuum, evidenced by their apparent chemical and rheologic similarities.

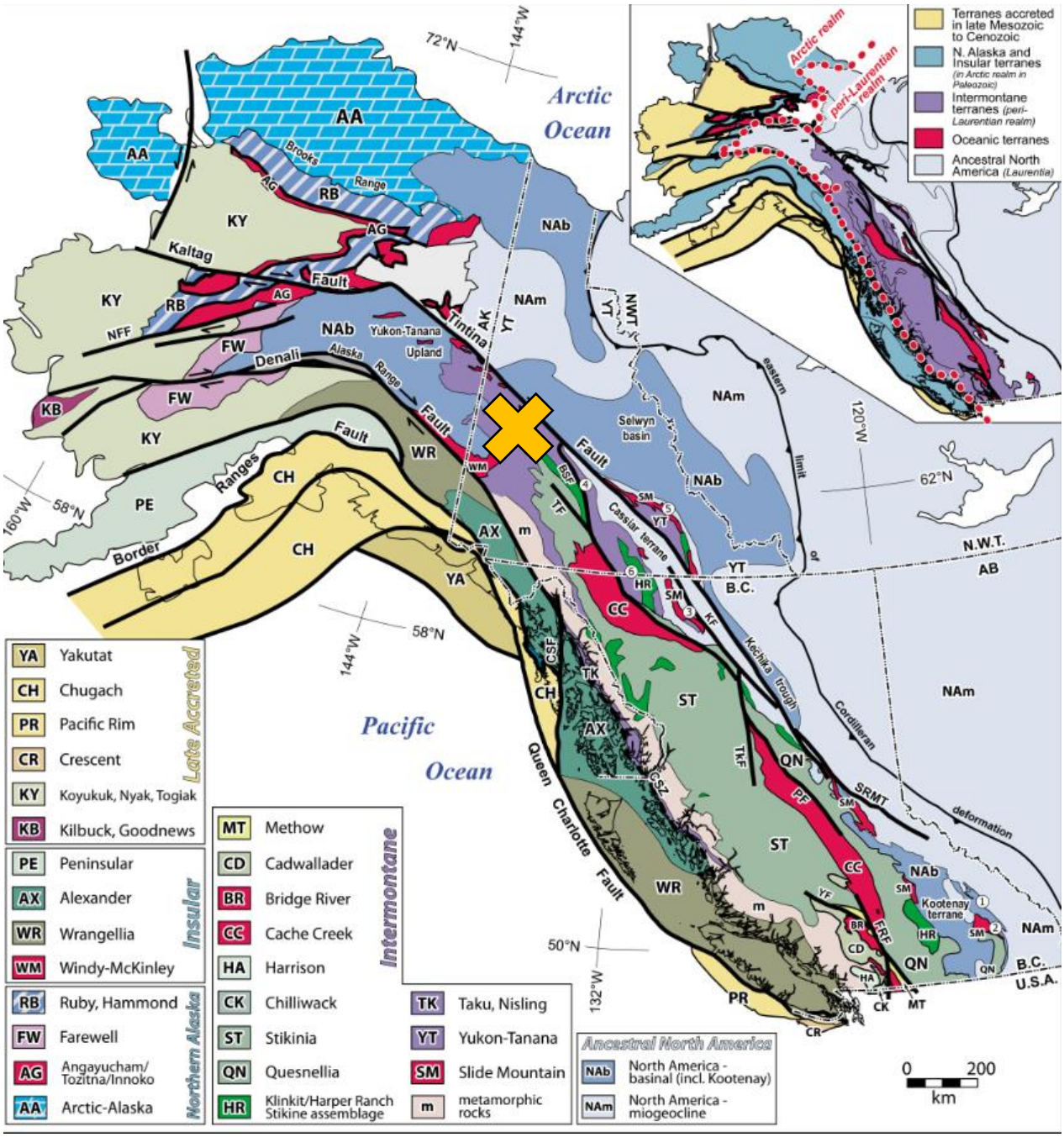

Figure 1: Terrane ordering of Northwestern Cordillera, modified from Colpron et al., 2007. The yellow X represents our study area within the Yukon-Tanana terrane, which is shown in more detail in Figure 2. This terrane is bounded by two dextral faults, in the north by the Tintina fault and in the South by the Denali fault.

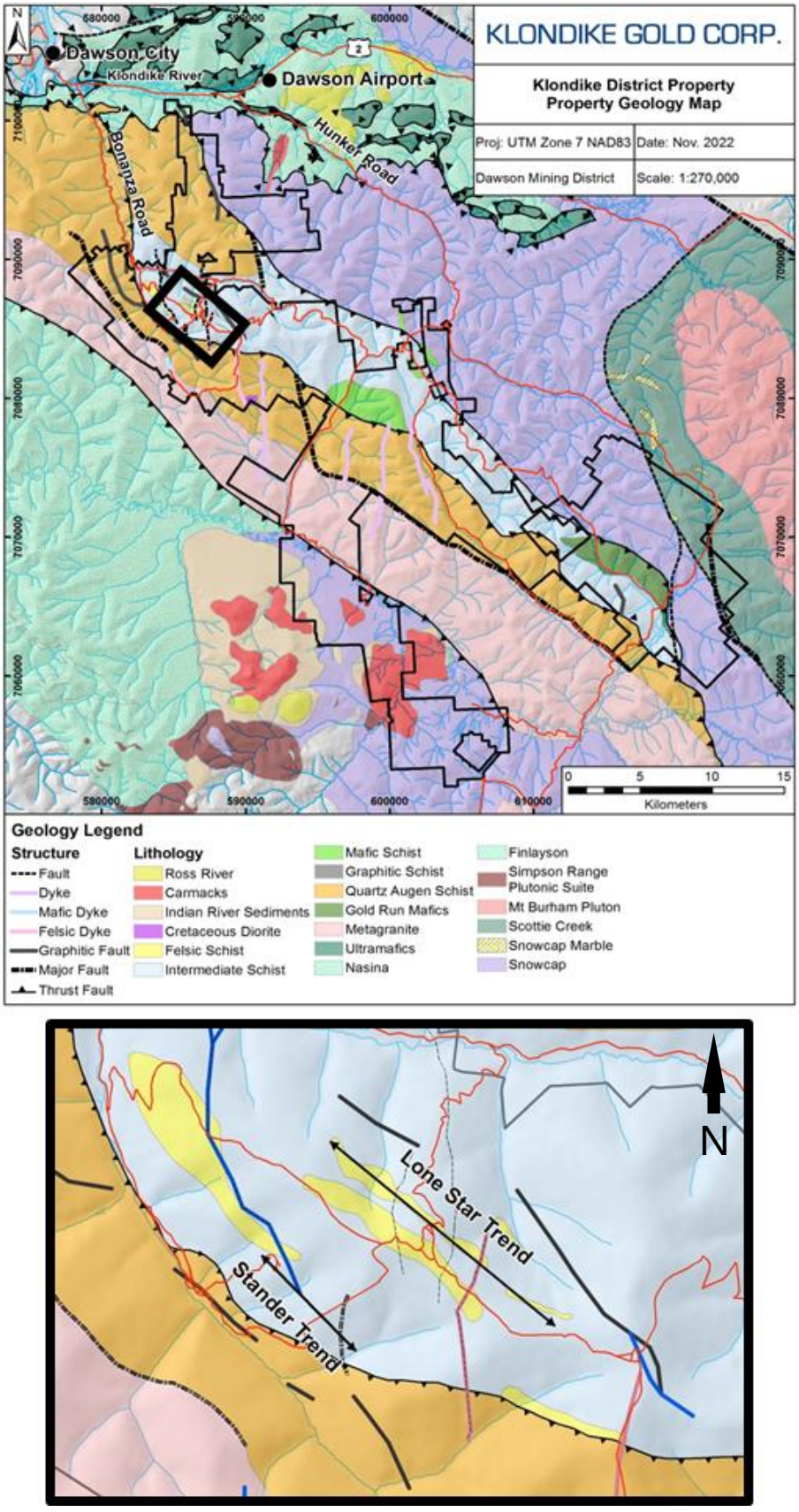

Figure 2: Property map provided by Klondike Gold Corp, 2022. Inset shows study area of interest; the light blue unit is QMS or intermediate schist, yellow being MQ or felsic schist, and the orange/brown unit to the south being quartz-augen-schist. Red lines are roads, dark gray lines are graphitic faults, and blue lines are late igneous dykes.

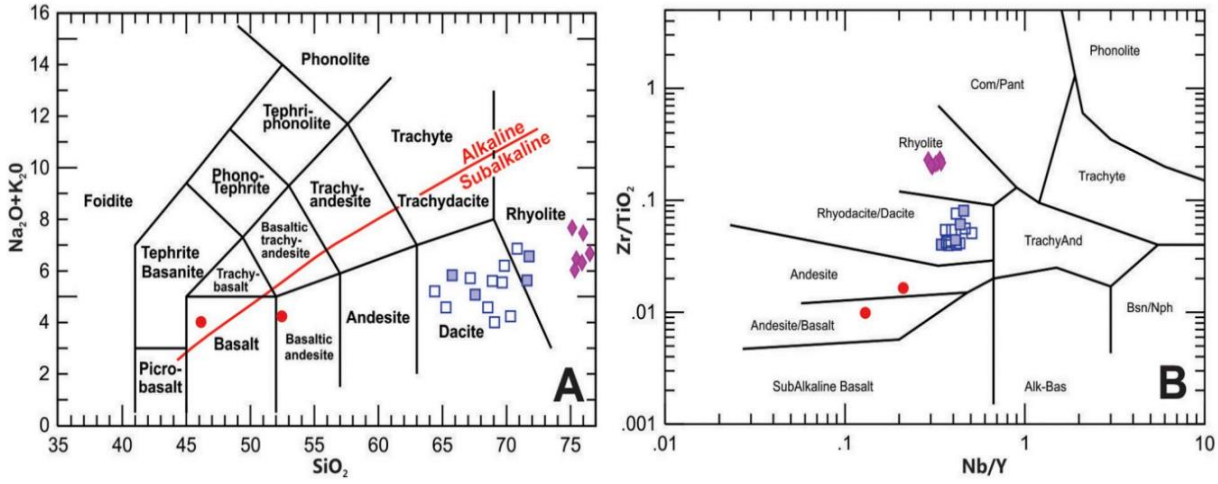

Figure 3: Bulk composition plots. A: total alkalis over silica, with alkaline/subalkaline boundary. B: Zr/TiO_2 over Nb/Y ratio; MQ as pink diamonds, QMS as open blue squares and QCMS as blue squares, with two "mafic schist" samples in red; from Mortenson et al., (2019).

The first documentation of gold mineralization was published early (McConnell, 1905) as occurring in a series of discordant quartz veins. During the time that the Boulder-Lode mine was operational in the early 20th century, gold was also documented to be schist-hosted (MINFILE 115O 180). Detailed descriptions of both disseminated mineralization (Mackenzie, 2007b) and observed quartz veining have since been published (Grimshaw, 2018). In a study on fluid inclusions in quartz veins, Rushton et al. (1993) concluded that mineralizing fluids had a strong meteoric input; however, Grimshaw (2018) points out that the paragenetic sequence for these quartz veins was incomplete, with 4 distinct phases being identified and only the last being associated with gold. He also reconciles gold in schist with gold in quartz veins to a single event in which fluid diffused into host units while being channeled through structural weaknesses in the schist packages. The general lack of broad structural focusing could contribute to the pervasiveness of gold mineralization in some sections of schist where gold-bearing quartz veins are not present (Grimshaw, 2018).

1.4 Sulfidation in orogenic systems

In any metamorphic suite, a variety of processes can affect the formation of an observed sulfide assemblage. The existence of possible syngenetic mineralization of a VMS (Very-Massive-Sulfide) is system noted in part of the property (Mackenzie et al., 2008), so we can consider the role this might have on our system first. Since we did not analyze any samples from

observed sulphide lenses, we can only speculate on this being a potential source for remobilized gold locally. There is evidence that gold in its native form can be sourced from deforming pyrites in a VMS deposit (Huston et al., 1992), but this process is limited by the actual concentration of gold dissolved in the pyrite (Grimshaw, 2018). Other elements may be released and transported as well during deformation, which, if involved in later crystallization of pyrite, could act as a source indicator; but, without any chemical constraints on actual trace element concentrations in this system, it is difficult to tell what this effect would be in practice. Being of the bulk composition rhyolite-dacite (Fig 3) (Mortenson et al., 2019), more generalized syngenetic pyrite formation is also a possibility to consider. Just as with our possible VMS pyrites, it is difficult to consider the effects of this strictly, as whole-rock trace element compositions remain poorly constrained for the region. While none of our samples contained obvious evidence of relict internal sulfide grains, this could be due to the small sample size and pervasive regional recrystallization (Beranek & Mortenson, 2011) erasing original grain-scale textures, and we may have just missed mapping a grain that displayed this type of internal structure. If syn-genetic pyrite was present in high concentrations within our host rocks and textures have been erased by overprinting sulfide events, we would expect chemically unique core trace-element patterns in most grains, assuming these relict pyrites would be preferred nucleation sites for any mineralizing fluid.

During orogeny, sulfide assemblages may be generated from mobilized fluids or metamorphic reactions, or sometimes by the same processes, be altered from their original state. There are 5 distinct deformation events documented as distinct fabrics and structures in this region (Mackenzie et al., 2008): an original S1 foliation, a regionally recrystallizing S2 fabric, a variably pervasive S3 crenulation fabric, D4 kink and fold structures, and D5 extensional faulting. It has been suggested that events correlated to S1-S3 fabrics generated negligible pyrite growth, but D4 and D5 events had potential for sulfide generation (Mackenzie et al., 2008). Due to the dynamic nature of these events, we could expect deformational or strain indicators to accompany observed textures for pyrites of this genesis. Taking possible metal input from VMS sources (Mortenson et al, 2006; 2019) and the effects of regional recrystallization into consideration, it is important to consider how metamorphism could modify our assemblages. McDonald (1967) provides a description of the 5 broad effects one could expect: textural changes (i.e. deformation), mineralogical changes (i.e. replacement or alteration), mobilization of

elemental constituents, reaction with non-sulphides (i.e. host rock), or generation of sulphide accumulations. In describing sulfur liberation, Tomkins (2010) emphasizes the importance of deformation for mobilization of fluids; without it, fluids will not be effectively transported and are more likely to react in place.

Post-tectonic or post-metamorphic processes are the last area we need to address regarding pyrite generation for the samples considered. These are processes that are driven by fluid circulation and controlled by structural pathways, as such it is an appropriate time to discuss transport of gold in the same paragraph as often both are driven by a related mechanism. Gold is mostly commonly transported as $Au(HS)_2^-$ or $AuCl_2^-$ complexes (Loucks & Mavrogenes, 1999), or sometimes in complexes with S^{3-} (Pokrovski et al., 2022). Realistically, a range of factors affect gold speciation, however, such as temperature, salinity, pH, and oxygen fugacity, as well as the possibility of different species existing altogether (Pokrovski et al., 2014). Based on fluid-inclusion studies of quartz veins estimating temperatures ranging from 200-350^{o}C (Rushton et al., 1993), this is within the range suggested for stability of the $Au(HS)_2^-$ complex (Loucks & Mavrogenes, 1999); however, it is suggested that S^{3-} speciation could be prevalent in the lower range of these temperatures, especially at higher acidities (Pokrovski et al., 2022). Considering a case in which gold would be transported via $Au(HS)_2^-$ during a change in fluid conditions, pyrite is precipitated, fixing sulfur and by association precipitating gold. In these systems, arsenic is often required as a requisite substitution to incorporate Au into the pyrite lattice (Reich et al., 2005). Commonly substituting for sulfur in pyrite, there is debate upon what exactly causes the observed arsenic correlation with gold, but some proposed ideas are: the chemical adsorption of $Au(HS)_2^-$ complexes on As-enriched faces, structural distortion to accommodate the larger Au^+ atom, or that they are simply controlled by the same precipitation mechanisms (Reich et al., 2005; Pokrovski et al., 2014). While gold may be transported as other species (such as $AuCl_2^-$) in fluids (Pokrovski et al., 2014) at Lone Star, an observed lack of dissolved gold could also be achieved in an arsenic limited system.

A common question for the genesis of pyrite in orogenic systems is one of sufficient sulfur. Many studies commonly favour metamorphic devolatization as a mechanism, which is the result of pyrite breakdown to pyrrhotite + S^{2-} during greenschist-amphibolite facies metamorphism coupled with the dehydration of chlorite/muscovite to generate mobilizing fluids (Zhong, 2015;

Tomkins, 2010; Phillips & Powell, 2010). This model is highly sensitive to pressure and temperature, with ideal conditions achieved where metamorphic conditions can be high-T and low-P at depth, optimally during compression or transpression (Tomkins et al., 2010). Mineralization in Lone Star is thought to occur sometime between the end of D4 deformation in the Jurassic, during transition from compressional D4 deformation to D5 extension active by the Cretaceous (Allan et al., 2013), which could realistically provide P and T conditions like the suggested ideal (Tomkins et al., 2010). Thus, this may be a significant process at depth in the Lone Star deposit, with fluids being focused up through regional structures to form discordant quartz veins while percolating through permeable schist layers (Grimshaw, 2018). In general, the tendency toward upward migration by hydrothermal fluids is due to them often being one third as dense as host rocks (Tomkins, 2010). As well as sulfur, we should also consider the source of iron for our pyrites. Grimshaw (2018) suggests pyrite is mainly growing as a mechanism of ilmenite breakdown. This process commonly produces rutile and titanite as products along with pyrite/pyrrhotite (generalized FeS) but requires interaction from sulfur (either as S_2 or H_2S, to produce pyrite with Fe) and calcium (Ca^{2+} to form titanite) to produce this assemblage (Angiboust & Harlov, 2017).

2 Methods

2.1 Sample Selection

The first criterion for selecting the samples analysed in this study was that pyrite grains were unaltered, which was mainly controlled by the combined factors of highly penetrative surface weathering and variable hydrothermal alteration associated with discordant veins. After this, sampling selection was determined around the basic goals of acquiring representative geologic units from high- and low-grade ore zones in both the Lone Star and Stander zones (Figure 2) with as many different pyrite occurrences as possible. We acknowledge our observations are not comprehensive on pyrite textures, as it was beyond the scope of this project to capture all possible occurrences due to the complexity of this deposit.

On site outside of Dawson City, YT, we took 16 drill core samples, of which 6 were finally selected for detailed analysis, and are listed in Table 1. Half are from the Lone Star zone, the other half from the Stander zone (Figure 2). Two of the Lone Star samples (LS17-91, LS19-287A, B) and two Stander samples are hosted within pyritic QMS (intermediate schist) with the other Lone Star sample (LS20-379) hosted within low-grade MQ (felsic schist). The last sample considered was taken from the Stander zone (EC22-481) containing pyrite grains hosted in an ankerite-quartz vein. Figure 2 provides the map of the region where samples were taken, with a close-up of Lone Star and Stander trends.

Table 1
Summary of sample information

Hole / Sample ID	Interval (m)	Collar easting	Collar northing	Provisional units[1]	Pervasive Structures	Types	Modal Py[2]	Au assay (ppm)
LS17-91	25.2-25.37	587006.25	7086149.66	QMS (intermediate schist)	S2, minor S3	Py1,Py2	3%	4.28
LS20-379	32.51-32.61	586986	7086100	MQ (felsic schist)	S2	Py2	0.5%	<0.01
LS19-287 (A,B)	45.14-45.33	587406	7085990	QMS (intermediate schist)	S2, S3 overprinting	Py1,py2	2%	5.69
EC19-259	72.25-72.5	585078.735	7085713.298	QMS (intermediate schist)	S2	Py2	2%	0.53
EC19-333	62.35-62.45	585066.598	7085695.118	QMS (intermediate schist)	S2, S3 overprinting	Py1,Py2	2%	4.43
EC22-481	21.48-21.67	585068	7085673	QMS (intermediate schist)	vein, S2 on edge	Py2,Py3	0.5-1%	n/a[3]

Notes:
1) Refer to full petrographic descriptions which can be found in appendix B
2) Values are approximate, as abundance was estimated visually
3) At the time of this project, assays have yet to be published. In the field, free gold was noted in the same vein system as this sample.

2.2 Sample preparation

Samples were selected and cut into quarter-core segments of roughly 10-20 cm in length on-site at Klondike Gold's camp in the Callison industrial district outside of Dawson City. Further work at Dalhousie University (DAL) produced chips from chosen samples that were mounted in epoxy in 1" rounds, then ground to expose sample surface and polished with 1- and 0.3-micron alumina. Additional polishing was done with colloidal silica at the Saint Mary's University (SMU) sample preparation facility.

Textures were documented first using a reflected light microscope in the petrology lab at DAL. Samples were then prepared by carbon coating in-house and examined for textural and mineralogical features using a TESCAN MIRA 3 LMU Variable Pressure Schottky Field Emission Scanning Electron Microscope (SEM) at SMU. The SEM is equipped with an 80 mm^2 X-max Oxford Instruments EDS detector and a back-scattered electron (BSE) detector. Semi-quantitative mineral analysis was performed using INCA software. A sample voltage of 20 kV, beam current of 0.2 nA and approximate working distance of 17mm were used for both EDS spot analysis and general imaging. Two of our samples were imaged with the SEM function on a JEOL JXA-8200 Electron Probe Micro-Analyzer (EPMA) at DAL, using a beam voltage of 15kv and approximate working distance of 15mm.

2.3 LA-ICPMS

Two sets of trace element analysis were performed: spots and maps. Analyses were performed at the LA-ICPMS facility in the Health and Environments Research Centre Laboratory at Dalhousie University. The system uses a frequency quintupled Nd:YAG laser operating at 213nm, coupled to a Thermo Scientific iCAP Q ICPMS quadrupole mass spectrometer with He flushing the ablation cell to enhance sensitivity (Eggins et al., 1998). Spot analyses were performed over two sessions. Laser conditions employed are: a repetition rate of 10 Hz, a spot size of 25um and a laser output of ~10 J/cm^2. Our first run had standard warmup/wash times of approximately 25s and 40s, with shorter than average ablation times of approximately 7-10s. The second session adhered to the same general settings aside from an increased laser output to ~15 J/cm^2, with warmup/washout times of ~20s and ~60s but performed longer ablations of ~60s. Times are approximate, as the second set of data was acquired in a manual triggered mode for spot acquisition, due to software issues. Combined sessions generated

a total of 108 core-rim spot analyses, acquired on 44 grains overall. The first session generated 76 analyses on 39 grains, measuring the following isotopes: ^{59}Co, ^{61}Ni, ^{63}Cu, ^{65}Cu, ^{75}As, ^{77}Se, ^{78}Se, ^{82}Se, ^{99}Ru, ^{100}Ru, ^{101}Ru, ^{103}Rh, ^{105}Pd, ^{105}Pd, ^{108}Pd, ^{107}Ag, ^{109}Ag, ^{121}Sb, ^{123}Sb, ^{125}Te, ^{126}Te, ^{128}Te, ^{130}Te, ^{185}Re, ^{188}Os, ^{189}Os, ^{190}Os, ^{191}Ir, ^{193}Ir, ^{194}Pt, ^{195}Pt, ^{197}Au, ^{206}Pb, ^{207}Pb, ^{208}Pb, ^{209}Bi. The second session measured an additional 5 grains and validated 11 grains from the first analysis. In the second session, isotopes were restricted to those found to be above detection limits based on the results of the first session. These included: ^{59}Co, ^{60}Ni, ^{63}Cu, ^{65}Cu, ^{75}As, ^{77}Se, ^{82}Se, ^{107}Ag, ^{109}Ag, ^{121}Sb, ^{123}Sb, ^{197}Au, ^{208}Pb, ^{209}Bi, and added ^{66}Zn, ^{67}Zn, ^{68}Zn. Data for all runs is provided as an excel sheet in the supplementary material. A final session with the LA-ICPMS generated 4 trace-element maps, considering the element suite: ^{55}Mn, ^{59}Co, ^{60}Ni, ^{65}Cu, ^{66}Zn, ^{82}Se, ^{75}As, ^{109}Ag, ^{121}Sb, ^{125}Te, ^{197}Au, ^{205}Tl, ^{208}Pb, ^{209}Bi.

For spot analyses, standards were analysed twice on MSS5 (crystalline iron sulfide; Dare et al., 2010) and NIST610 (silicate glass; Jochum et al., 2007) before and after every 20 unknowns. Maps were acquired using a grid of parallel line-scans at a spacing of 20 microns and a 20 micron beam diameter, with a 10 Hz repetition rate and output of ~13 J/cm^2. MSS5 was used to standardize all isotopes except ^{59}Co, which used NIST610. It should be noted that a nominal value of 13 +/- 1 ppm was used in MSS5 as the standard for Zn, so values should be taken to be semi-quantitative. Additionally, there was no lab standard for ^{205}Tl; thus, for mapping purposes, its value is reported in counts per second (cps) with a lower threshold of one cps. The reason for this inclusion was for ease of integration into a larger dataset being assembled by colleagues at the University of Toronto. To correct ablation yields, we calibrated to stoichiometric Fe in pyrite (~46.67%), as semi-quantitative SEM work showed samples were typically close to this concentration.

Data was reduced and maps were generated using the data reduction software iolite4 (Paton et al., 2011), and maps were combined with SEM images in photo-editing software. Maps were processed first using a mask to crop the images to areas with only >1,500,000 cps of ^{32}S, then an in-program interpolation function was used to smooth edges. Resolution on the LS17-91 map was poor due to the small area of analysis, and an accurate overlay was difficult to achieve. For mineral abbreviations when assembling maps, the authors referred to Whitney et al. (2010).

3 Results

3.1 Summary of pyrite texture

Three primary pyrite types were identified based on grain-fabric relationships: syn-tectonic (Py 1), post-tectonic (Py 2), and vein pyrites (Py 3). Only one sample of Py3 was taken from the Stander zone, and while of clearly different phase, there were no cross-cutting relationships between the veins and matrix pyrite.

Syn-tectonic Py1 show signs of strain in the form of fracturing (occasionally forming shear planes and elongations along fabric planes) or other deformation textures, shown in Fig 4 in both LS17-91 and LS19-287A. These grains are most often found in association with S3 fabrics and typically contain phengite, quartz, albite, apatite, or monazite inclusions, reflecting the matrix mineralogy. Post-tectonic, Py2, grains occur as idioblastic porphyroblasts that cut whichever fabric they are hosted in, S2 or S3, and contain the same variety of inclusions as the syn-tectonic grains (Fig 4). Pyrites in LS17-91 seem to represent a different phase of Py2 since pyrites in this sample are finer grained on average and tend to form small, clustered aggregates but are nonetheless idioblastic. In terms of overall abundance, Py2 types are much more common than Py1 types. Py3 is only found in cross-cutting quartz veins, so they cannot be accurately compared in terms of proportions to sulphides in wall-rock. While generally related to S3 fabrics only, Py1 examples may also occur that record deformation from S2 recrystallization, particularly in areas where relationships are difficult to resolve, or from the speculated reactivation of S3 during D4 deformation (Smith & Cragg, 2022). Grains varied in size from the 10s of micron scale to over 0.5 mm in some samples, but typically averaged around 500 um. The largest pyrite crystals were found in EC19-259 on average, with the smallest being found in LS17-91.

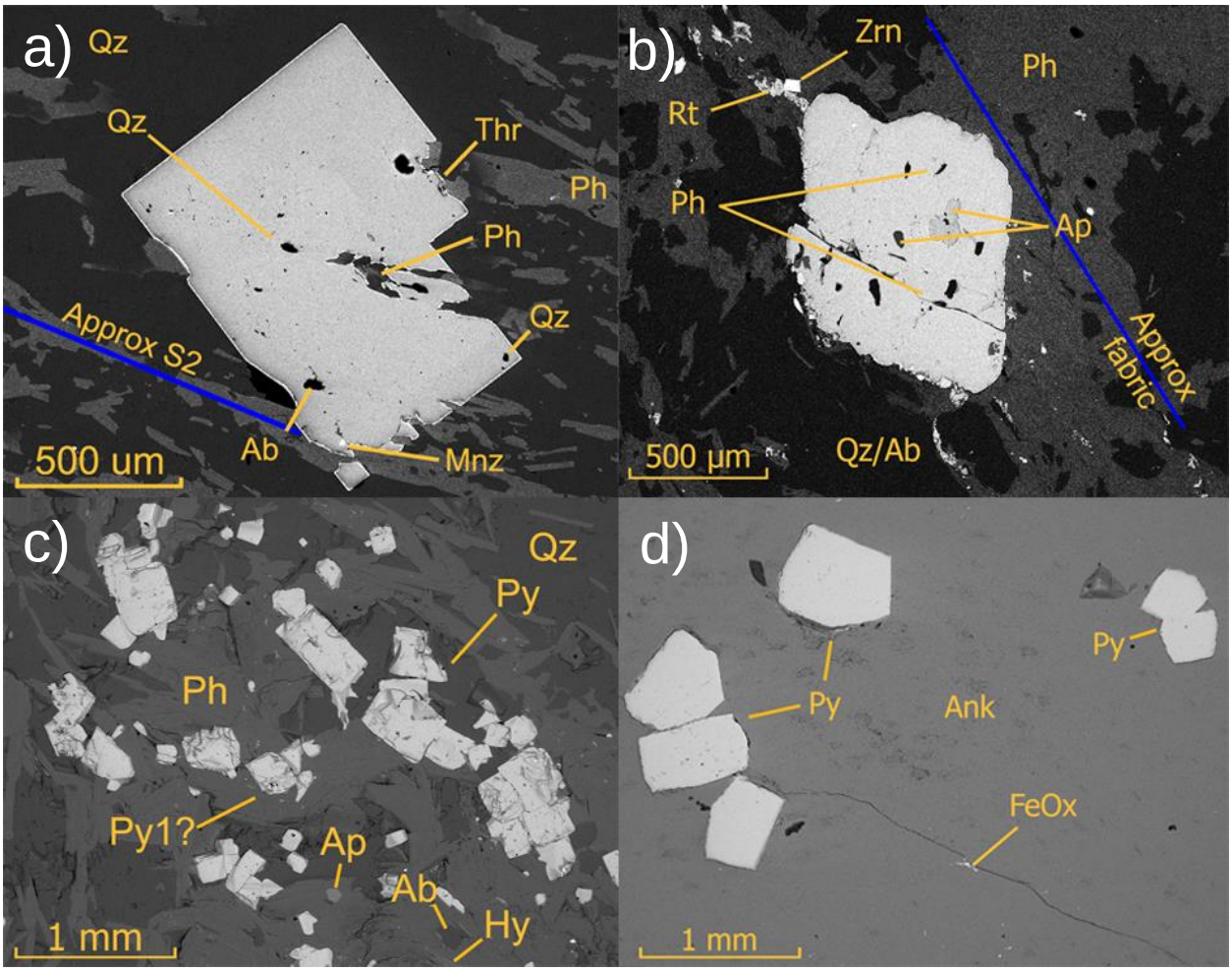

Figure 4: Backscattered electron (BSE) images displaying pyrite textural types. a) LS20-379, py2 grain cross-cutting S2; b) LS19-287A py1 grain with deformation textures inline with S3 fabric; c) LS17-91 fine grain py2 disseminated along S2 structures and a possible py1 grain. d) EC22-481 vein py3 coexisting with ankerite. Note it was difficult to reconcile the difference between S2 and S3 fabrics for LS19-287 in RFL and SEM.

3.2 Matrix mineralogy

The EDS on the SEM at SMU allowed for interrogation of the matrix mineralogy. Detailed lithologic reports are included in the appendix and list prominent primary and secondary matrix minerals observed in our grains. Notably, although chlorite was noted in hand samples, and described previously for the same lithologies investigated here, it was not identified in thin section. Additionally, LS20-379 contained interstitial barite in significant proportions compared to other samples and generally lacked apatite, the latter also being generally coarser

grained in EC samples. The only other sample where barite was noted was trace in EC19-333 and interstitial in the Py-hosting ankerite-quartz vein of EC22-481.

3.3 Spot analysis

A summary of trace element data from spot analyses is provided in Table 2, displaying averages of all grains (regardless of type) from a given sample, counts, and concentration of the isotopes considered in our final mapping run. LS19-287 produced several pieces with good pyrite exposures, and two pieces were run for analysis (A/B sections), but both are lumped into the same overall sample. Due to the uneven distribution of many chalcophile elements, Fig 6 is restricted to only consistently detectable isotopes.

Represented as an upper crust (UC) normalized diagram, Fig 6 shows the general chemical distribution of pyrites between types as well as zones. This normalization was performed to remove effects of fractionation from general formation of the crust as well as to eliminate the natural sawtooth effect that would occur if absolute concentrations were plotted. Average upper crust data was retrieved from compositions estimated by Rudnick & Gao (2003). There exists an apparent fractionation between both zones (Lone Star vs Stander) and pyrite types (Py1 vs Py2 vs Py3). General observations can be summarized as follows: Co/Ni ratios tend to be lower in EC (Stander) pyrites, EC Py2 grains tend to be enriched in Co, Ni, As and Se comparatively but depleted in Pb and Bi, and lastly that Py2 seems to record the highest overall variation in terms of trace element composition.

Zinc values for py1 weren't analyzed in the first run that captured this pyrite type, so detection limits from the second run are used to keep plots continuous. Also, Cu values from this run are reported at detection due to the potential for surface contamination introduced during polishing, which was observed to cause distinct Cu-peaks at the beginning of runs, and analysis times weren't long enough to correct for this. Au, Ag, Se, Sb, Te and Bi are mainly at detection for our samples; however, our mapping efforts determined that these elements are not usually

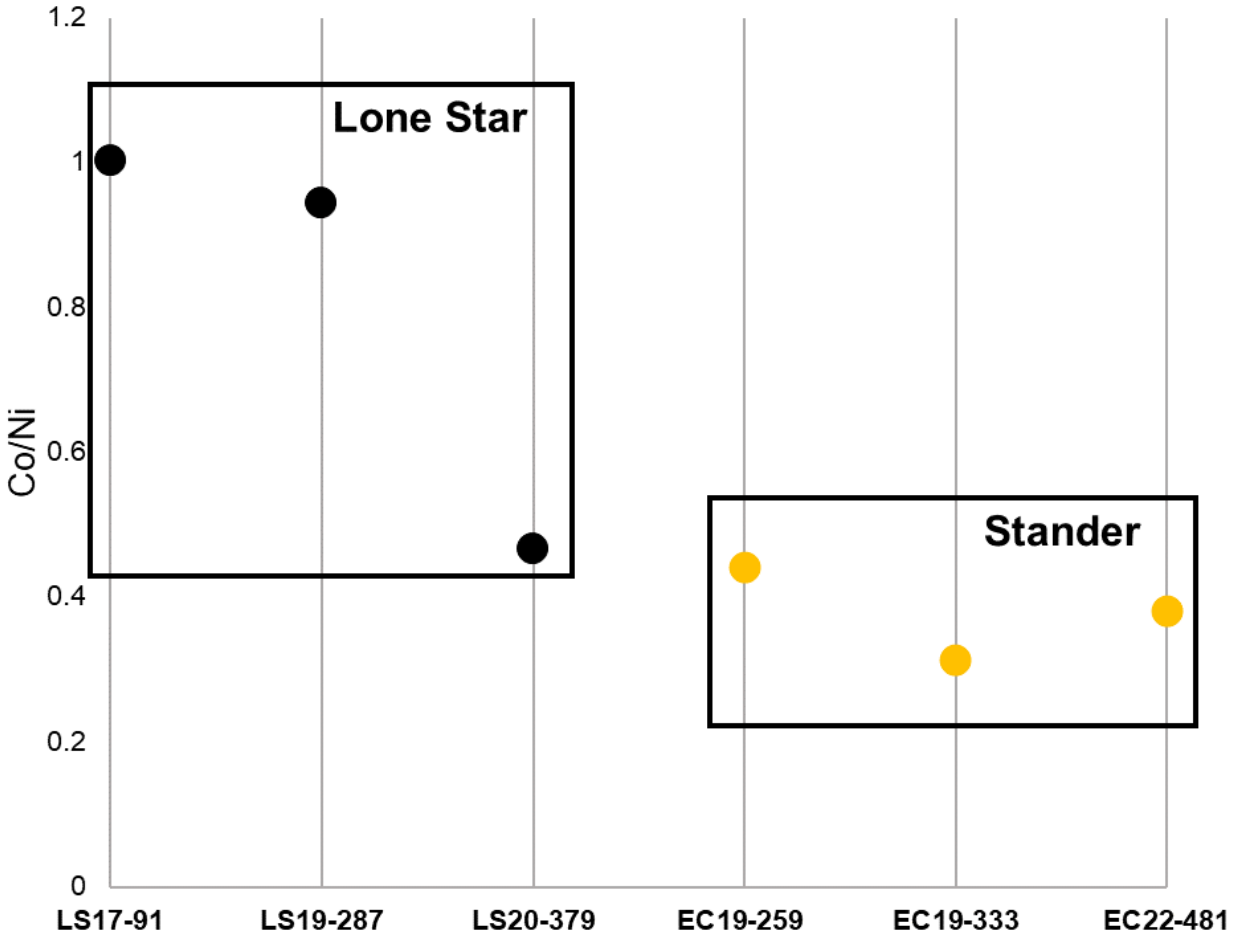

Fig 5: Cobalt/Nickel ratio plot for our 6 samples. Lone Star pyrites plotted in black are seen to be generally more enriched and closer to unity excluding LS20-379, which is closer to the more depleted Stander grains in yellow.

present as a dissolved component (except for Se in EC19-259) in sampled pyrites and are typically often hosted in inclusions when present. Pb and Bi tend to be enriched together (Fig 6), and this is possibly an effect of incidental sampling of galena or bismuthide inclusions (Fig 7a). Galena, chalcopyrite, sphalerite, tellurides and arsenian pyrite were all documented as inclusions during descriptions (appendix B), thus making Cu, Ag (common in Cpy), Zn, and As all subject to the same possible effect. Figure 7 illustrates this inclusion effect with time-resolved diagrams of spot analyses from the second session, comparing an inclusion-bearing pyrite from LS17-91 (Fig 7a) with a homogenous one from LS19-287A (Fig 7b). Intergrowths of secondary minerals are commonly found as inclusions in sampled pyrites, with accessory sulfides like galena, chalcopyrite, and sphalerite as common modes, which results in inclusion peaks overlapping (Fig 7a). This can be differentiated from internal zonation by patterns displayed by Co and Ni which display regular peaks that don't diminish significantly with ablation time (Fig 7a).

Table 2
Summary of trace element data averaged by sample, in ug/g, non-normalized

Sample ID	n[1]	^{59}Co	^{60}Ni	^{65}Cu	^{66}Zn	^{75}As	^{82}Se	^{107}Ag	^{121}Sb	^{125}Te	^{197}Au	^{208}Pb	^{209}Bi
LS17-91	6	92.9	92.6	11.6	1.10	7.23	17.4	0.563	0.225	nd	0.022	5.96	0.145
σ[3]		34.7	26.7	11.6	2.30	4.57	1.72	2.86	0.279	nd	0.039	1.09	0.542
LS19-287A	20	97.9	84.4	8.15	8.84	14.1	18.9	1.30	1.10	0.330	0.056	3.07	0.323
σ		74.1	44.8	7.71	0	8.01	4.29	0	0.945	0.070	0.006	4.57	0.335
LS19-287B	4	87.6	120.	1.57	0.874	8.77	16.3	0.484	0.236	nd	0.023	3.42	0.330
σ		32.5	63.6	0.624	0.094	0.649	0.307	0.376	0	nd	0.010	0	0
LS20-379	19	16.5	35.3	21.2	1.43	10.0	13.1	4.16	1.82	5.12	0.088	32.9	0.088
σ		15.23	25.9	0	0	6.84	2.29	4.09	1.69	0	0.068	39.4	0.06
EC19-259	20	273.	619.	0.650	1.35	792.	62.1	0.156	0.138	0.458	0.050	0.856	0.038
σ		365.	959.	5.07	0.446	605.	34.6	0.021	0.645	0.189	0.024	5.12	0.018
EC19-333	16	232.	742.	nd	nd	91.6	25.5	bdl	0.270	0.733	bdl	0.445	0.034
σ		495.	535.	nd	nd	113.	9.88	bdl	0	0.378	bdl	0.414	0.012
EC22-481[2]	19	130.	341.	nd/bdl	nd/bdl	1240	25.4	0.904	0.408	0.663	0.066	1.29	0.048
σ		34.0	24.1	nd/bdl	nd/bdl	156.	3.58	0.279	0.283	0.211	0.022	2.51	0
Dec 9 LOD		0.509	8.62	nd	nd	1.04	8.317	0.929	0.176	0.249	0.049	0.041	0.035
Jan 24 LOD		0.052	0.151	0.339	0.648	0.206	1.642	0.087	0.035	nd	0.009	0.046	0.014

Notes:
1) n: number of analyses, bdl: below detection limit, LOD: limit of detection
2) bdl: below detection limit, in EC22-481 Cu and Zn were not detected for the majority of grains analyzed, but were below detection in two grains checked in the second session of analysis
3) Standard deviation (σ) values are high due to there being a significant range in data as a result of being composites of core-rim spot analyses. We know that internal structures can be complex between pyrite types and various inclusions are common, either of which could influence spot data in a given sample.

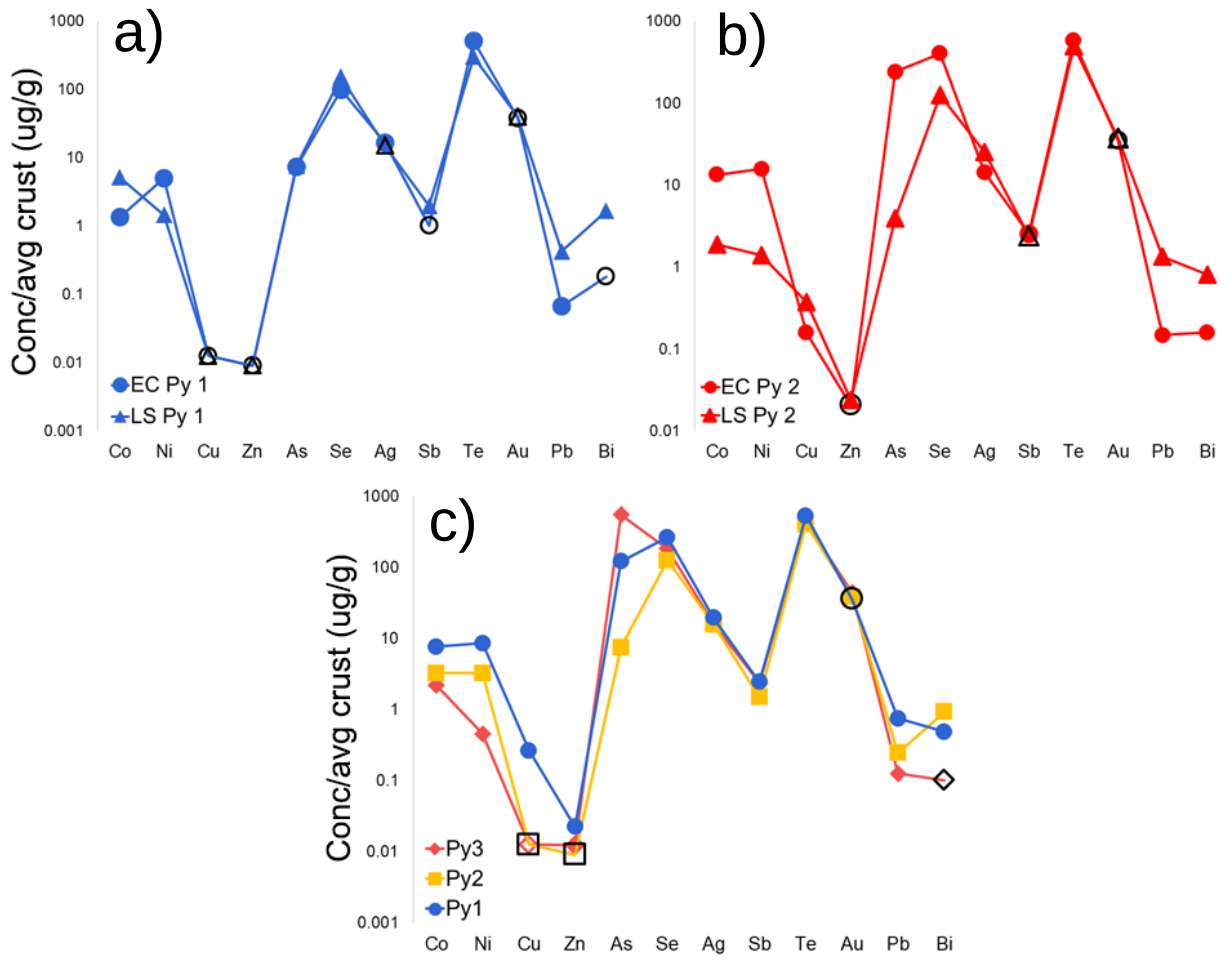

Figure 6: UC-normalized diagrams from spot data, with comparisons between zones by pyrite type in a) and b), and a general comparison between types in c). Sample zone was found to have the biggest effect on the trace element pattern in this case, but there still exists an overall variation between types, especially in terms of Co, Ni, and As. Black outlined symbology represents where elements are plotted at limits of detection.

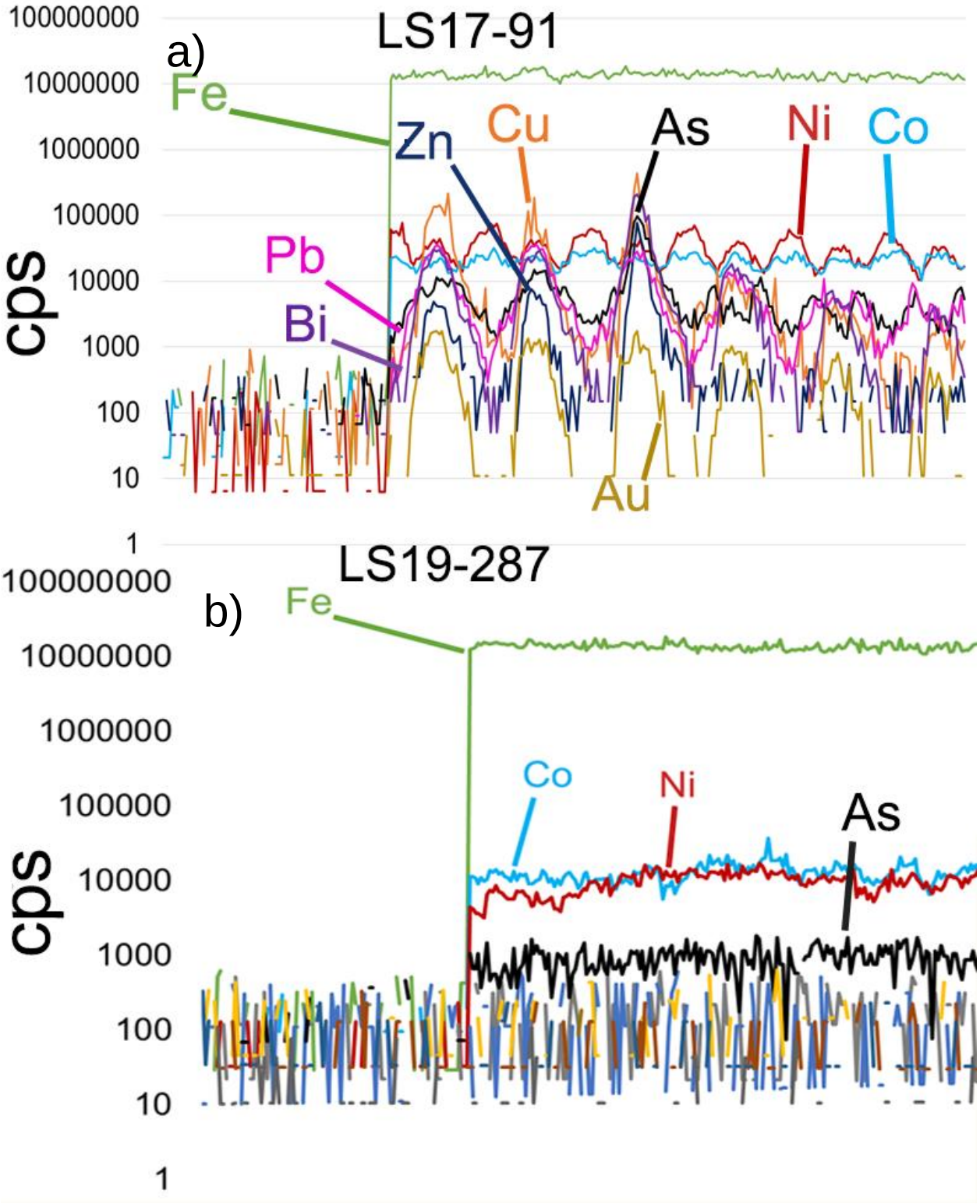

Fig 7: Time-resolved trace element diagrams. a) Core of an LS17-91 Py2 showing pattern of Pb, Bi, As, Zn, Cu inclusions likely as an intergrowth, with Ni and Co plotted to show growth zoning; b) core of LS19-287A grain showing homogenous fractions of Co, Ni, As, with all other elements at detection

3.4 LA-ICPMS mapping

A total of four grains were mapped, with one sample from the Stander zone (EC19-259) and three from the Lone Star zone (LS17-91, LS19-287A, LS20-379). EC19-259, and LS20-379 are post-tectonic Py2 grains and LS19-287A is a syn-tectonic Py1 grain. All grains have strong internal patterns except for LS17-91, and Co is used to illustrate these features in Fig 8. This is a good element to evaluate across the maps, as it is detectable in all samples and commonly displays well-developed zoning in other pyrite occurrences (Mathieu, 2019). LS19-287A (Fig 8d) has a Co-enriched, Ni-depleted core (appendix A) surrounded by cycles of uneven Co-enrichment, with an overprinted rim displaying a zoned composition of Co/Ni. The center of this grain also appears weakly enriched in As (Appendix A). This grain also appears to record a deformation structure in its zonation pattern (Fig 8c). EC19-259 displays two modes of zonation: internally segregated sectors of different concentration and a distinct overprint defined by cyclic layers of Co. This sample can also be differentiated by its comparatively high As concentration, as well as being the only grain displaying dissolved Se. The grain mapped in LS20-379 was selected due to it being the only grain detected with significant Au in previous spot analysis, and this work revealed that this was a result of accidentally intersecting an Au-Te inclusion rather than gold as a dissolved component.

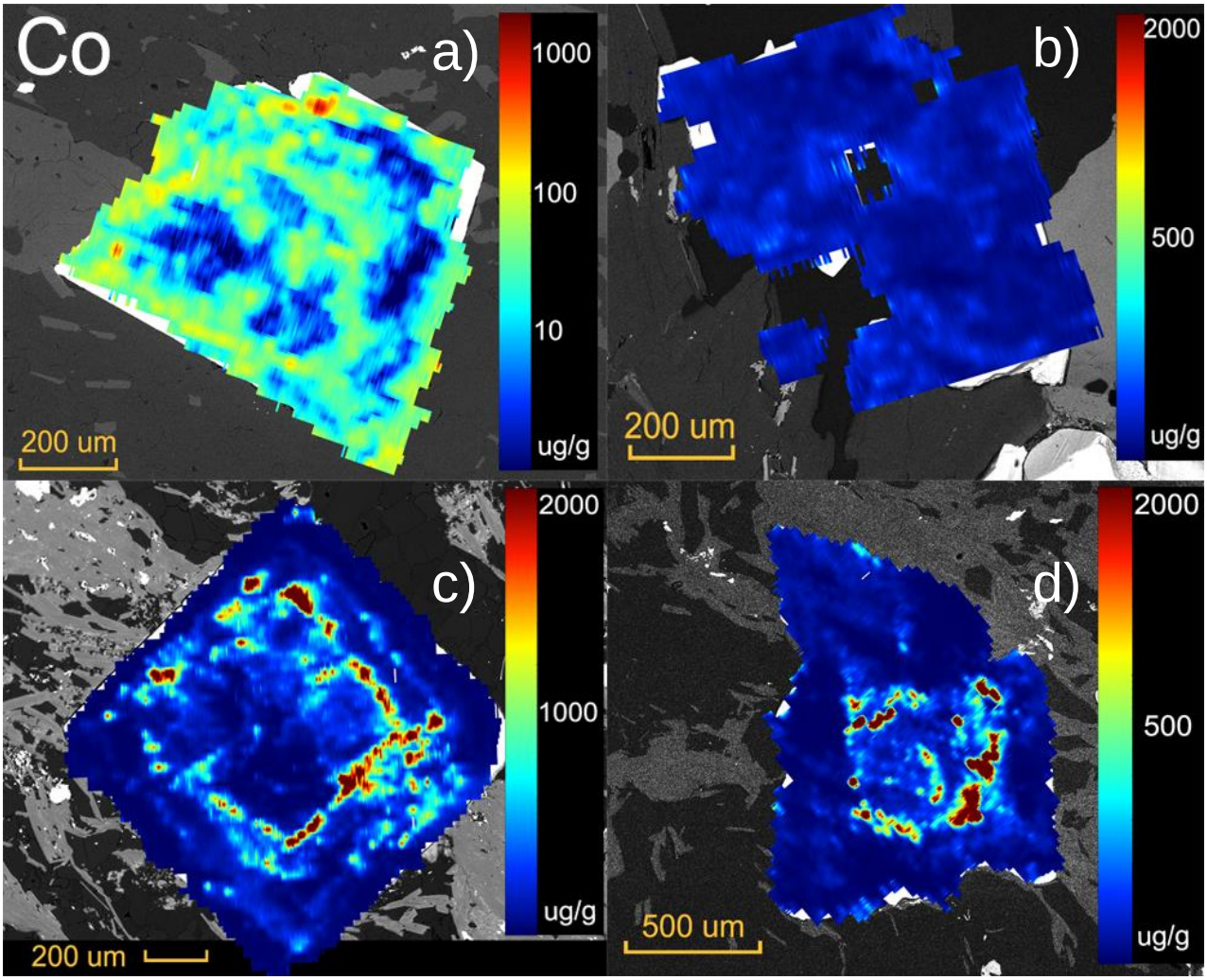

Fig 8: LA-ICPMS imaging results as Co overlain onto BSE images. a) LS20-379 Py2, uses log scale due to Co depletion; b) LS17-91 Py2, mostly homogenous chemical structure; c) EC19-259 Py2; d) LS19-287A Py1, with core elongate parallel to D3 structure

In LS20-379 (Fig 8a), Co is depleted relative to other samples, so a logarithmic scale is used to accentuate zoning. This grain has the lowest contents of Ni and Co and possesses a core enriched in Cu and Tl and contains abundant inclusions of Pb, with minor Au-telluride inclusions (appendix A). The zoning in the rim of this grain is defined exclusively by Co and Ni. Lastly, LS17-91 (Fig 8b) appears to have no systematic internal structure regarding concentration of Co or any other element. This sample also displays a connection with Au-bearing telluride minerals, however, which occur along the margins of grain boundaries (Appendix A).

The only consistent elements present as a dissolved fraction across grains seems to be Co, Ni, and As, except for Se in EC19-259 while all other measured elements are seen to generally behave as inclusions. Figure 7a gives an example of observed inclusions, in this grain likely present as an intergrowth of secondary minerals, displayed using time resolved ablation diagrams. Galena is represented by spikes in Pb and Bi, with Cu and Zn peaks representing chalcopyrite and sphalerite inclusions respectively. Lastly, As spikes represent inclusions of arsenian/arsenopyrite of a different phase, with small gold peaks either associated with the As-mineral, as a telluride or in native form. Unfortunately, for the second session we did not determine Te concentrations, so we cannot conclude the presence of telluride minerals. Comparing to Fig 7b, this grain represents the more homogenous population we observe, and only partitions Co, Ni, and As as a dissolved phase. In Fig 7a, Co/Ni peaks are taken to represent growth zoning and are independent of inclusion peaks.

These results can be used to refine and expand previous sample classifications, and possible subtypes can be suggested for Py2 types. LS17-91 could represent Py2a, defined by an overall depletion and lack of internal chemical structure, smaller grain size, and general tendency to form aggregates. Au-Ag-Bi-Te inclusions are observed along this grain's boundary, which could suggest a correlation with this pyrite type. LS20-379 could represent Py2b, which has an overall depletion in elements relative to other pyrite types but retains internal zonation. This grain is also notable for being host to Au-telluride inclusions in its structure, which, when compared to LS17-91, could possibly indicate that Py2b is generated as an overgrowth on Py2a grains. Lastly, a Py2c could be present in EC19-259, which has a more-regularly zoned pattern, dissolved Se, and a more significant proportion of dissolved As. It's important to consider that there could be zoning in all grains observed, but sections may not always cut through the centre of the crystal structure, as well as the fact that Py3 types were not mapped at all.

3.5 Region of interest plots

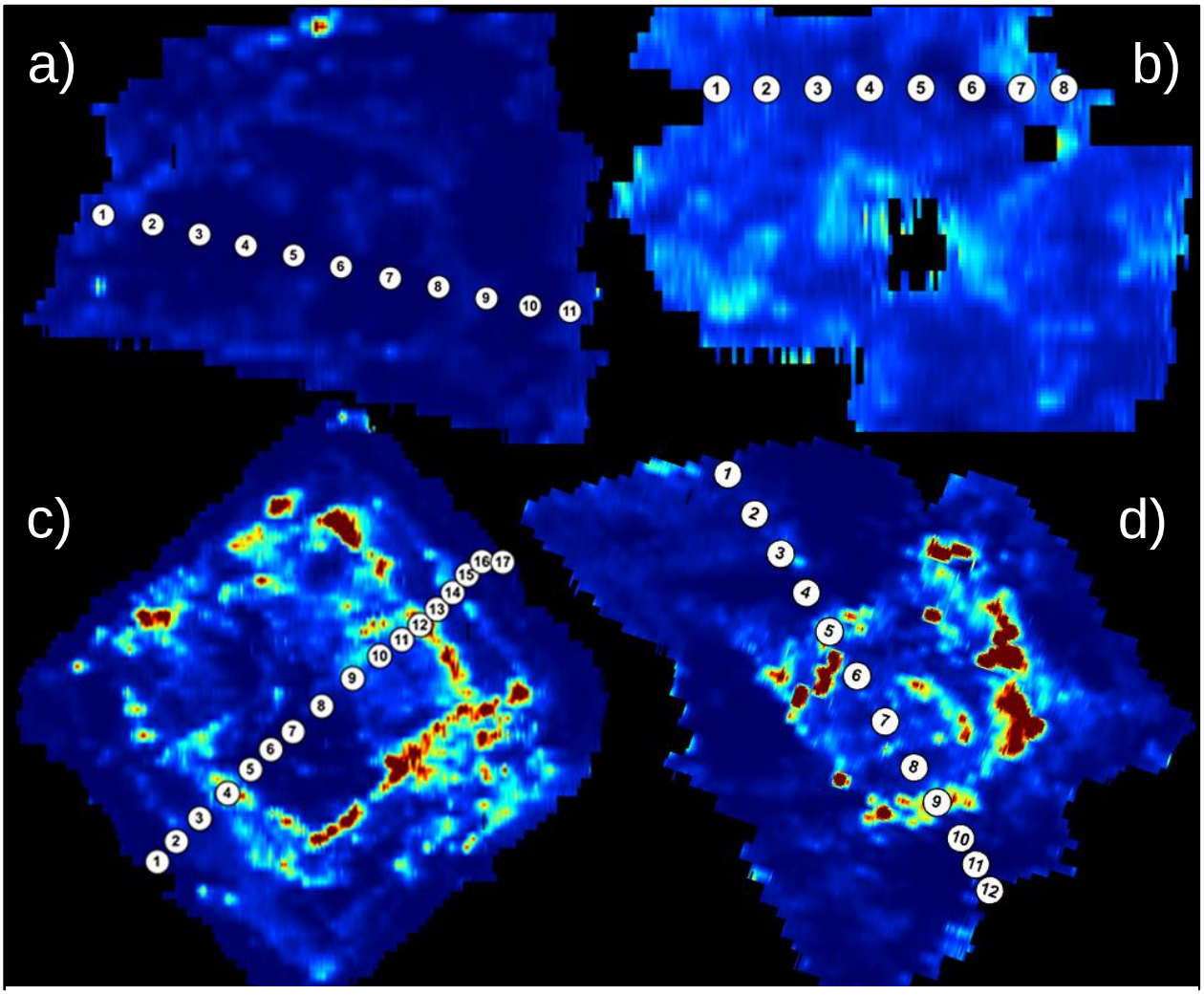

Fig 9: Region of interest transects overlaid on Co laser images. a) LS20-379; b) LS17-91; c) EC19-259; d) LS19-287A. Each spot is ~25um, but markers are enlarged for visibility. In Fig 10, not all EC19-259, LS19-287A or LS20-379 points were used, to declutter plots.

Another way to investigate the mapping data is by using the built-in region of interest tool in iolite4 to generate detailed compositional information from traverses across individual grains, mimicking a line of spot analyses (Fig 9). Each region is equivalent to a 25um spot, although the markers in Fig 9 are larger than their true spot size for the purpose of readability. Data was extracted then filtered to remove values below detection (due to the nature of line-scans overlapping matrix and inclusions, average limits of detection were higher than for a typical spot analysis). After this, UC-normalized diagrams were generated for each given traverse, using the suite of elements that we used for LA-ICPMS mapping (Fig 10). This method allows for quantification of data that would otherwise rely on visual interpretation. In Fig 10,

patterns of enrichment are shown between core and rim zones, with patterns colour-coded to show differences. Commonly, cores display slightly different enrichment patterns than rims, with EC19-259 (Fig 8c) displaying the most general variation when data is plotted this way and LS20-379 showing the least variation (Fig 10a). This implies core-rim relationships are most distinct in LS20-379 and least distinct in EC19-259.

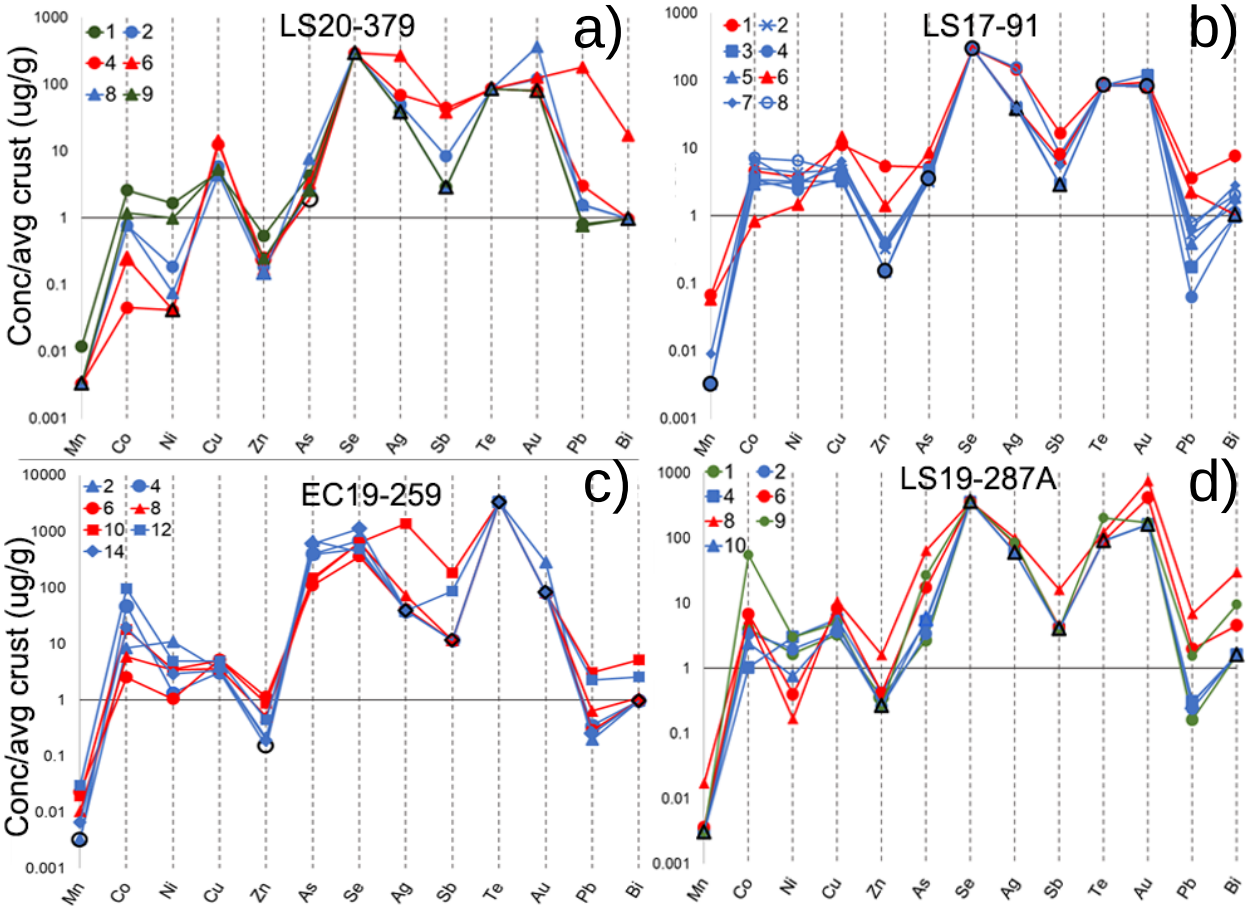

Fig 10: UC-normalized diagrams generated from region of interest transects (Fig 9). Representative points were chosen to be graphed to reduce clutter. Blue represents rim measurements and red represents cores, with green used to point out anomalous patterns in LS19-287A and LS20-379. Black outlined symbology represents where elements are plotted at LOD.

Considering LS17-91 (Fig 8b, 9b) first, this Py2 grain displays no discernable zonation and does not have any major inclusions in its structure. In Fig 9b, across the traverse in Fig 9b, we can see this pyrite has an effective consistent chemical patten aside from Spots 1 and 6, which have elevated Tl, Mn, Cu, Zn, and Pb concentrations. Additionally, Spot 6 is relatively depleted in Co, Ni, and Bi.

The next grain we consider is LS19-287A, which displays strong internal zonation (Fig 8d, 9d) and is elongated parallel to local S3 crenulation. This grain possesses a distinct core-rim relationship and what appears to be deformation recorded in the overgrowth. Cores (Spots 6 and 8) are elevated in Zn, As, Sb, Au, Pb, and Bi relatively while being depleted in Ni. Spots 5 and 9 are transitional core-rim measurements and are relatively enriched in Co but otherwise fall intermediate to core-rim measurements. When looking at Fig 10d, there appears to be distinct patterns, but all plots follow the same general trends of enrichment.

Our only mapped Stander zone sample, EC19-259 (Fig 8c, 9c), also shows strong internal zonation (Fig 8c) and is the only sample with dissolved Se. Core-rim relationships are of a similar history to LS19-287A, shown in Fig 10c with lines generally falling on a continuous chemical spectrum with some grouping between populations of core patterns (red) and rim patterns (blue). Cores are enriched relative to rims in Tl and Co with the rims enriched relatively in Se, Ni, and As. Internal zoning in EC19-259 (Fig 8c) is displayed as “sectors” in the core overgrown by layers of cyclic composition.

Lastly, considering LS20-379 (Fig 8a, 9a), this grain has another unique pattern in our UC-normalized diagrams. In Fig 10a, three distinct groups are defined; firstly, Spots 1 and 9, which are rim measurements enriched in Co and Ni but depleted in Sb and Pb. Next, Spots 4 and 6 define a core enriched in Tl, Cu, Ag, Sb, Pb and Bi but depleted in Co and Ni. Lastly, Spots 2 and 8 represent the boundaries of the core with the rim and are intermediate other than being enriched in Co and Ni. Like LS19-287A, this grain also displays distinct patterns between core, rim, and transitional zone.

4 Discussion

4.1 Compositional evolution of pyrite in the Lone Star deposit

There are a variety of pyrite textures present in this deposit, likely due to the wide range of conditions one can encounter in metamorphic terranes. Evidence of this complexity is present in our four mapped grains (Fig 8), in that each presents a slightly different history of growth. The main observations that are recorded are that LS17-91, LS19-287A, and EC19-259 show evidence of mainly growing from an evolving fluid, while LS20-379 displays evidence for a discrete core that is overgrown.

First, LS17-91 is our most homogenous grain, which could originate because of either a fixed, perhaps externally buffered, fluid composition or by homogenization of zoning due to elemental diffusion. Notably, Au telluride inclusions are present along part of the grain boundary of this pyrite. The mechanism of homogenization first runs into issues when trying to explain the idioblastic nature of this grain. To maintain these grain boundaries for the extent of homogenization with an interacting fluid, there would have to be little active deformation, and thought is that sulfidation is intimately related with deformation events (Mackenzie et al., 2008). Secondly, to partition elements into the pyrite structure, we would require a fluid in disequilibrium to our grain, which should result in reaction textures occurring along relict grain boundaries. It is still theoretically possible, however, that at sufficiently high levels of metamorphism that all original trace elements were forced out of the pyrite structure (Beluosov et al., 2016), but both with dominance of regional retrograde lower-mid greenschist facies metamorphism and the described grain boundary issue, we should still expect some kind of reaction texture in the structure to be imprinted during the formation of this grain's final shape. Assuming an external fluid source, low arsenic content may have prevented gold from being taken up as a dissolved component, and a slow cooling history could have resulted in efficient exclusion of impurities, resulting in observed inclusions along the grain boundaries.

The only pyrite displaying this type of internal deformation structure, LS19-287 contains patterns of zoning in its rim parallel to the deforming fabric (Fig 8d), which implies a syngenetic relationship with the event that created S3 fabrics (or possibly D4 if reactivated). Coinciding with strong visual core-rim zonation displayed by this grain, inspection of the traverse (Fig 9d) data in Fig 10d shows a slight distinction between core-rim groups, but spots generally adhere to the same chemical patterns. This texture could be hard to reconcile as a single evolving fluid

lacking a consistent diffusion gradient; however, in a system driven by large-scale cyclic metamorphic processes, multiple pulses of the same fluid is not unreasonable and could be driven by mechanisms such as the fault-valve model (Sibson, 1992). Considering indications of growth during deformation, the core, which appears more idioblastic than the grain boundaries, probably grew prior to or near the beginning of deformation. It is unlikely this core was derived from a significantly different fluid to the rim that overgrew it, as we would probably expect more drastic elemental differences. The main identifiable differences in element phases is higher concentrations of Co, Zn, As, Sb, Au, Pb, and Bi in the core, with a rim that is relatively depleted in the same elements. A potential growth history for this pyrite could have involved two pulses of a similarly buffered fluid, with a first event growing a relatively idioblastic core and a second, more depleted phase nucleating on the first without significantly reacting with or altering the core.

Considering EC19-259, this grain is sampled from the Stander zone, which is shown to have a slightly different pyrite chemistry to Lone Star (Table 2, Fig 6). This sample also had a core-rim texture but did not record any deformation; core "sectors" could be produced by a period of rapid growth preferentially incorporating elements along faces and grain boundaries, later overgrown by slightly slower, but still relatively fast crystallizing, cyclic layers. As shown in Figure 10c, there is a slight core-rim distinction in patterns, but plots generally follow the same chemical continuum, and we can invoke a similar process as with formation of LS19-287A. With absence of evidence for significant reaction between core and rim either texturally or chemically, we explain the observed elemental differences (i.e., weak Se enrichment in rim) as reflective of changes in the source fluid, which was buffered similarly for both growth period.

Lastly, LS20-379 represents the last expression of pyrite growth in this study. Like LS19-287A and EC19-259, a core-rim relationship exists in this sample (Fig 8a), but element relations are slightly different. Cores are enriched in Tl, Cu, Ag, Sb, Pb and Bi but depleted in Co and Ni, with rims being enriched in Co and Ni and depleted in all other elements. This data seems to represent a chemically distinct core interacting with an overgrowing fluid, which based on visual interrogation of maps, appears to have reacted and dissolved at parts of the original grain boundary. Core-rim enrichment patterns in this grain could provide evidence for recrystallization, and distinct enrichment patterns in Fig 10d at the contact between the core and the overgrowth (Spots 2 and 8) could help support this theory. In the same figure, these

transitional points also lie generally intermediate to plotted core-rim measurements, which could possibly imply a period of re-equilibration with reacting fluid. As previously mentioned, distinct core-rim elemental relations are usually considered when dealing with recrystallization due to the variable liberation of trace elements from the core (Large et al., 2009; Belousov et al., 2016; Steadman et al., 2021), and textures in this pyrite provide evidence of such. Furthermore, this sample contained Au-tellurides in its structure near the internal core-rim boundary, and an original grain could have provided a nucleation site for these inclusions.

4.2 Trace element partitioning in Lone Star and Stander pyrites

Typically, when pyrite trace element partitioning is investigated, it is in the context of ore genesis, usually in the form of a variety of chalcophile element associations. Lone Star deviates from the ideal of typical systems in some ways, such as the lack of Au-As correlation or significant dissolved trace elements in general. Due to the its ability to facilitate gold substitution, Au-As is probably the most common elemental pair considered in ore pyrite (Steadman et al., 2021; Belouosov et al., 2016; Large et al, 2011; Large et al. 2009). Another common correlation in these systems is between Au-Te (Keith et al, 2020; Belouosov et al., 2016), and could be considered like an endmember to the OGD system (Belouosov et al., 2016). While we do observe Au-bearing tellurides in our minerals, these are common in pyrites among diagenetic, hydrothermal, and magmatic deposits (Large et al, 2011; Velasquez et al., 2014; Stromberg, 2019) and alone don't supply enough evidence to strongly link sulfidation with gold in our case. There are occurrences, however, where most of the gold in a deposit is trapped in inclusions (Belouosov et al., 2016), but we do not observe them in high enough concentration for this to be the case.

In general, As concentrations are low, and present both homogenously and as inclusions (likely arsenian pyrite) in the pyrite structure, with levels being elevated in EC-series samples (Table 2) compared to LS-series samples. The map for EC19-259 (Appendix A) is the only grain to show significant As zonation; however, there remains no correlation with gold in either maps or spot samples. This sample lacks inclusions as well, and this implies the mineralizing fluid for this pyrite either carried very little gold or transported it via a complex other than $Au(HS)_2^-$. The observed distinctions between sample series vary depending on the zone the pyrite was sampled from. EC-series samples are in the Stander zone of the Lone Star deposit, roughly 1km from the

main Lone Star trend and largely within more chlorite-rich QMS schist, bordering with the quartz-augen-schist member, another subdivision of the Klondike Assemblage. Following the general model of fluids sourced at depth circulating through our units, these chemical differences could represent an offshoot from the main trend or be a result of fluid reacting with slightly different bulk compositions, which could be evidenced by higher prevalence of matrix chlorite in this unit as observed in hand sample.

Another common technique to investigate sulfidation in gold-bearing systems is to look at the Co/Ni ratio, which has been shown to be relatively robust technique for differentiating deposit types (Bajwah et al., 1987, Gregory et al., 2015, Belousov et al., 2016). This method is not entirely accurate due to the complexity of these systems; contradictions exist in the literature regarding values for certain conditions of pyrite formation. For example, in Bajwah et al. (1987), diagenetic pyrite is seen to contain <100 ug/g Co and have a Co/Ni < 1, but real Co and Ni uptake is modified by factors such as redox state or presence of organic-rich material (Gregory et al., 2015) and could cause shifts in this ratio. VHMS deposits seem to remain relatively consistent between studies, however, displaying anomalously high Co/Ni ratios, typically in two populations of >5 and >10 (Bajwah et al., 1987; Belousov et al., 2016). Orogenic systems are also seemingly well constrained, and typically have Co/Ni ratios <1 (Belousov et al., 2016). Within the Lone Star deposit, Co/Ni ratios in samples are controlled by zone, with LS20-379 as an outlier to this, as shown in Figure 4. Starting with samples from the Lone Star zone, LS17-91 and LS19-287A, both in QMS, have relatively similar Co/Ni ratios effectively at unity, being 1.00 and 0.945 respectively. LS20-379 has the overall lowest Co/Ni concentrations (Table 2) and a Co/Ni ratio of 0.467. Ratios for Stander zone samples are lower overall, with EC19-259 at 0.441, EC19-333 at 0.313, and EC22-481 at 0.481. These results are in line with previously mentioned estimates for typical orogenic systems (Belousov et al., 2016); however, differences between zones remains unexplored. This could be a result of several factors: different fluid phases, differences in effects of rock-buffering, or different histories of fluid-mixing (for example, fluids permeating through Stander zone mixed with a larger proportion of some meteoric fluid enriched in Ni relative to Co). Considering Fig 8, fractionation of Co/Ni within a given grain must be acknowledged. In a system with a limited budget of both Co and Ni, assuming wall-rock scavenging would be minimal in generally felsic compositions (Mortenson et al., 2019), patterns of fractionation between these two is expected due to their similar

elemental characteristics and would be governed by both fluid and crystal partitioning of trace elements. Unfortunately, literature is limited on the latter in hydrothermally driven systems, so exact mechanics of this remain unknown. In general, enrichment patterns mimic each other across each region measurement, except for differences recorded in LS20-379.

5. Concluding Remarks

This study classifies and quantifies several aspects of a few textures of pyrite on the Lone Star deposit property. Major findings can be summarized as follows: pyrites are variably affected by deformation, sometimes display multi-generational growth zoning, have generally low As contents and Co/Ni ratios, do not generally incorporate chalcophiles (incl. Au and Ag) as a dissolved fraction, and instead contain a variety of these trace elements within inclusion populations. Lack of a dissolved gold component as well as the overall low population of gold-bearing inclusions effectively eliminates pyrite as an in-situ source for metals in this deposit. Sulfidation timing and fabric associations deviate slightly from past observations (Mackenzie et al., 2008), due to observations of LS20-287A being associated with D3 structures, though it is also possible for these structures to have been reactivated by later events. Future work regarding pyrite analysis should aim to be more comprehensive regarding textural type, and to try to determine and investigate units that could be potential source rocks for gold in the area. Lastly, it is evident that whatever major gold-bearing phase is present precipitates temporally later than fluids which grew pyrite, but whether this is due to multiple fluid pulses, effects of different Au-speciation, or some other chemical constraint on the system is unknown, and investigating these variables could be a direction for future work.

6. References

ANGIBOUST, S., & HARLOV, D. (2017). Ilmenite breakdown and rutile-titanite stability in metagranitoids: Natural observations and experimental results. *American Mineralogist*, **102(8)**, 1696–1708. https://doi.org/10.2138/am-2017-6064

ALLAN, M. M., MORTENSEN, J. K., & COOK, N. (2013). Chapter 4: Magmatic and metallogenic framework of West-Central Yukon and Eastern Alaska. *In* Tectonics, Metallogeny, and Discovery: The North American Cordillera and Similar Accretionary Settings (COLPRON, M., BISSIG, T., RUSK, B.G., THOMPSON, J. F. H., eds.). Society of Economic Geologists, Inc. (111-168)

BAJWAH, Z. U., SECCOMBE, P. K., & OFFLER, R. (1987). Trace element distribution, Co:Ni ratios and genesis of the Big Cadia iron-copper deposit, New South Wales, Australia. *Mineralium Deposita*, **22(4)**, 292–300. https://doi.org/10.1007/BF00204522

BERANEK., L. P. & MORTENSON, J. K. (2011). The timing and provenance record of the Late Permian Klondike orogeny in northwestern Canada and arc-continent collision along western North America. *Tectonics*, **30**, TC5017, doi:10.1029/2010TC002849

BELOUSOV, I., LARGE, R. R., MEFFRE, S., DANYUSHEVSKY, L. V., STEADMAN, J., & BEARDSMORE, T. (2016). Pyrite compositions from VHMS and orogenic Au deposits in the Yilgarn Craton, Western Australia: Implications for gold and copper exploration. *Ore Geology Reviews*, **79**, 474–499. https://doi.org/10.1016/j.oregeorev.2016.04.020

CHAPMAN, R. J., MORTENSEN, J. K., CRAWFORD, E. C., & LEBARGE, W. (2010). Microchemical Studies of Placer and Lode Gold in the Klondike District, Yukon, Canada: 1. Evidence for a Small, Gold-Rich, Orogenic Hydrothermal System in the Bonanza and Eldorado Creek Area. *Economic Geology*, **105(8)**, 1369–1392. https://doi.org/10.2113/econgeo.105.8.1369

DARE, S. A. S., BARNES, S.-J., & PRICHARD, H. M. (2010). The distribution of platinum group elements (PGE) and other chalcophile elements among sulfides from the Creighton Ni–Cu–PGE sulfide deposit, Sudbury, Canada, and the origin of palladium in pentlandite. *Mineralium Deposita*, **45(8)**, 765–793. https://doi.org/10.1007/s00126-010-0295-6

DICKINSON, W. R. (2004). Evolution of the North American Cordillera. *Annual Review of Earth and Planetary Sciences*, **32**, 13–45. https://doi.org/10.1146/annurev.earth.32.101802.120257

GREGORY, D. D., LARGE, R. R., HALPIN, J. A., BATURINA, E. L., LYONS, T. W., WU, S., DANYUSHEVSKY, L., SACK, P. J., CHAPPAZ, A., MASLENNIKOV, V. V., & BULL, S. W. (2015). Trace Element Content of Sedimentary Pyrite in Black Shales*. *Economic Geology*, **110(6)**, 1389–1410. https://doi.org/10.2113/econgeo.110.6.1389

GRIMSHAW, M. R. (2018). *Gold Mineralisation in the Lone Star area of the Klondike Gold District, Yukon, Canada* [Phd, University of Leeds]. https://etheses.whiterose.ac.uk/20012/

GROVES, D. I., GOLDFARB, R. J., GEBRE-MARIAM, M., HAGEMANN, S. G., & ROBERT, F. (1998). Orogenic gold deposits: A proposed classification in the context of their crustal distribution and relationship to other gold deposit types. *Ore Geology Reviews*, **13(1)**, 7–27. https://doi.org/10.1016/S0169-1368(97)00012-7

JOCHUM, K. P., NOHL, U., HERWIG, K., LAMMEL, E., STOLL, B., & HOFMANN, A. W. (2005). GeoReM: A New Geochemical Database for Reference Materials and Isotopic Standards. *Geostandards and Geoanalytical Research*, **29(3)**, 333–338. https://doi.org/10.1111/j.1751-908X.2005.tb00904.x

JUTRAS, M. & KENWOOD, S. (2022). NI 43-101 Technical Report on the Klondike District Gold Project, Yukon Territory, Canada. Prepared for Klondike Gold Corporation by Ginto Consulting Inc.

KEITH, M., SMITH, D. J., DOYLE, K., HOLWELL, D. A., JENKIN, G. R. T., BARRY, T. L., BECKER, J., & RAMPE, J. (2020). Pyrite chemistry: A new window into Au-Te ore-forming processes in alkaline epithermal districts, Cripple Creek, Colorado. *Geochimica et Cosmochimica Acta*, **274**, 172–191. https://doi.org/10.1016/j.gca.2020.01.056

KNIGHT, J. B., MORTENSEN, J. K., & MORISON, S. R. (1999). Lode and placer gold composition in the Klondike District, Yukon Territory, Canada; implications for the nature and genesis of Klondike placer and lode gold deposits. *Economic Geology*, **94(5)**, 649–664. https://doi.org/10.2113/gsecongeo.94.5.649

LARGE, R. R., DANYUSHEVSKY, L., HOLLIT, C., MASLENNIKOV, V., MEFFRE, S., GILBERT, S., BULL, S., SCOTT, R., EMSBO, P., THOMAS, H., SINGH, B., & FOSTER, J. (2009). Gold and Trace Element Zonation in Pyrite Using a Laser Imaging Technique:

Implications for the Timing of Gold in Orogenic and Carlin-Style Sediment-Hosted Deposits. *Economic Geology*, **104(5)**, 635–668. https://doi.org/10.2113/gsecongeo.104.5.635

LARGE, R. R., BULL, S. W., & MASLENNIKOV, V. V. (2011). A Carbonaceous Sedimentary Source-Rock Model for Carlin-Type and Orogenic Gold Deposits. *Economic Geology*, **106(3)**, 331–358. https://doi.org/10.2113/econgeo.106.3.331

LOUCKS, R. R., & MAVROGENES, J. A. (1999). Gold Solubility in Supercritical Hydrothermal Brines Measured in Synthetic Fluid Inclusions. *Science*, **284(5423)**, 2159–2163. https://doi.org/10.1126/science.284.5423.2159

MACKENZIE, D., CRAW, D., & MORTENSEN, J. K. (2007a). Thrust slices and associated deformation in the Klondike goldfields, Yukon. *Yukon Exploration and Geology 2007*. 199-213

MACKENZIE, D., CRAW, D., MORTENSEN, J. K., & LIVERTON, T. (2007b). Disseminated gold mineralization associated with orogenic veins in the Klondike Schist, Yukon. *Yukon Exploration and Geology 2007*. 215-224

MACKENZIE, D. J., CRAW, D., & MORTENSEN, J. (2008). Structural controls on orogenic gold mineralisation in the Klondike goldfield, Canada. *Mineralium Deposita*, **43(4)**, 435–448. https://doi.org/10.1007/s00126-007-0173-z

MATHIEU, L. (2019). Detecting magmatic-derived fluids using pyrite chemistry: Example of the Chibougamau area, Abitibi Subprovince, Québec. *Ore Geology Reviews*, **114**, 103-127. https://doi.org/10.1016/j.oregeorev.2019.103127

MCCONNELL, B. A. (1905). Report on the Klondike gold fields. Geological Survey of Canada

MCDONALD, J. A. (1967). Metamorphism and its effects on sulphide assemblages. *Mineralium Deposita*, **2(3)**, 200-220. https://doi.org/10.1007/BF00201916

MINFILE, Y. updated 2019. Occurrence Number 115O 180. Yukon Geological Survey.

MORTENSON, J. K., DUSEL-BACON, C., HUNT, J., & GABITES, J. (2006). Lead isotopic constraints on the metallogeny of middle and late Paleozoic syngenetic base-metal occurrences in the Yukon-Tanana and Slide Mountain/Seventymile terranes and adjacent portions of the North American miogeocline. *In* Paleozoic Evolution and Metallogeny of Pericratonic Terranes at the Ancient Pacific Margin of North America, Canadian and Alaskan Cordillera (COLPRON, M & NELSON, J. L., eds.). Geological Association of Canada, Special Paper 45. 261-279

MORTENSEN, J. K., LIVERTON, T., & DODD, K. (2019). Chemostratigraphic constraints on the nature and origin of felsic schist units hosting stratabound and orogenic vein gold on Lone

Star Ridge, Klondike Gold District, Yukon. *Journal of Geochemical Exploration*, **204**, 112–130. https://doi.org/10.1016/j.gexplo.2019.05.011

NELSON, J., AND COLPRON, M. (2007). Tectonics and metallogeny of the British Columbia, Yukon and Alaskan Cordillera, 1.8 Ga to the present, *In* Mineral Deposits of Canada: A Synthesis of Major Deposit-Types, District Metallogeny, the Evolution of Geological Provinces, and Exploration Methods (Goodfellow, W.D., ed.,). Geological Association of Canada, Mineral Deposits Division, Special Publication No. 5, 755-791.

NELSON, J.L., COLPRON, M., PIERCEY, S.J., DUSEL-BACON, C., MURPHY, D.C. AND ROOTS, C.F., (2006). Paleozoic tectonic and metallogenic evolution of the pericratonic terranes in Yukon, northern British Columbia and eastern Alaska, *In* Paleozoic Evolution and Metallogeny of Pericratonic Terranes at the Ancient Pacific Margin of North America, Canadian and Alaskan Cordillera (Colpron, M. and Nelson, J.L., eds.). Geological Association of Canada, Special Paper 45, 323-360.

PATON, C., HELLSTROM, J., PAUL, B., WOODHEAD, J., & HERGT, J. (2011). Iolite: Freeware for the visualisation and processing of mass spectrometric data. *Journal of Analytical Atomic Spectrometry*, **26(12)**, 2508–2518. https://doi.org/10.1039/C1JA10172B

PHILLIPS, G. N., & POWELL, R. (2010). Formation of gold deposits: A metamorphic devolatilization model. *Journal of Metamorphic Geology*, **28(6)**, 689–718. https://doi.org/10.1111/j.1525-1314.2010.00887.x

PIERCEY, S. J., & COLPRON, M. (2009). Composition and provenance of the Snowcap assemblage, basement to the Yukon-Tanana terrane, northern Cordillera: Implications for Cordilleran crustal growth. *Geosphere.* **5(5),** 439-464.

POKROVSKI, G. S., AKINFIEV, N. N., BORISOVA, A. Y., ZOTOV, A. V., & KOUZMANOV, K. (2014). Gold speciation and transport in geological fluids: Insights from experiments and physical-chemical modelling. *Geological Society, London, Special Publications*, **402(1)**, 9–70. https://doi.org/10.1144/SP402.4

POKROVSKI, G. S., DESMAELE, E., LASKAR, C., BAZARKINA, E. F., TESTEMALE, D., HAZEMANN, J.-L., VUILLEUMIER, R., SEITSONEN, A. P., FERLAT, G., & SAITTA, A. M. (2022). Gold speciation in hydrothermal fluids revealed by in situ high energy resolution X-ray absorption spectroscopy. *American Mineralogist*, **107(3)**, 369–376. https://doi.org/10.2138/am-2022-8008

HUSTON, D. L., BOTTRILL, R. S., CREELMAN, R. A., ZAW, K., RAMSDEN, T. R., RAND, S. W., GEMMELL, J. B., JABLONSKI, W., SIE, S. H., & LARGE, R. R. (1992). Geologic and geochemical controls on the mineralogy and grain size of gold-bearing phases, eastern Australian volcanic-hosted massive sulfide deposits. *Economic Geology*, **87(3)**, 542–563. https://doi.org/10.2113/gsecongeo.87.3.542

REICH, M., KESLER, S. E., UTSUNOMIYA, S., PALENIK, C. S., CHRYSSOULIS, S. L., & EWING, R. C. (2005). Solubility of gold in arsenian pyrite. *Geochimica et Cosmochimica Acta*, **69(11)**, 2781–2796. https://doi.org/10.1016/j.gca.2005.01.011

RUDNICK, R. L., & GAO, S. (2014). Composition of the Continental Crust. In *Treatise on Geochemistry* (pp. 1–51). Elsevier. https://doi.org/10.1016/B978-0-08-095975-7.00301-6

RUSHTON, R. W., NESBITT, B. E., MUEHLENBACHS, K., & MORTENSEN, J. K. (1993). A fluid inclusion and stable isotope study of Au quartz veins in the Klondike District, Yukon Territory, Canada; a section through a mesothermal vein system. *Economic Geology*, **88(3)**, 647–678. https://doi.org/10.2113/gsecongeo.88.3.647

SIBSON, R. H. (1992). Fault-valve behavior and the hydrostatic-lithostatic fluid pressure interface. *Earth-Science Reviews*, **32(1)**, 141–144. https://doi.org/10.1016/0012-8252(92)90019-P

STEADMAN, J. A., LARGE, R. R., OLIN, P. H., DANYUSHEVSKY, L. V., MEFFRE, S., HUSTON, D., FABRIS, A., LISITSIN, V., & WELLS, T. (2021). Pyrite trace element behavior in magmatic-hydrothermal environments: An LA-ICPMS imaging study. *Ore Geology Reviews*, **128**, 103878. https://doi.org/10.1016/j.oregeorev.2020.103878

SMITH, J. & CRAGGS, S., (2022). Independent Technical Report for the Klondike District Gold Project, Yukon Territory, Canada. Prepared for Klondike Gold Corporation by SRK Consulting Inc, project number 3CK012.002.

VELÁSQUEZ, G., BÉZIAT, D., SALVI, S., SIEBENALLER, L., BORISOVA, A. Y., POKROVSKI, G. S., & DE PARSEVAL, P. (2014). Formation and Deformation of Pyrite and Implications for Gold Mineralization in the El Callao District, Venezuela. *Economic Geology*, **109(2)**, 457–486. https://doi.org/10.2113/econgeo.109.2.457

WHITNEY, D. L., & EVANS, B. W. (2010). Abbreviations for names of rock-forming minerals. *American Mineralogist*, **95(1)**, 185–187. https://doi.org/10.2138/am.2010.3371

ZHONG, R., BRUGGER, J., TOMKINS, A. G., CHEN, Y., & LI, W. (2015). Fate of gold and base metals during metamorphic devolatilization of a pelite. *Geochimica et Cosmochimica Acta*, **171**, 338–352. https://doi.org/10.1016/j.gca.2015.09.013

Appendix A: LA-ICPMS maps

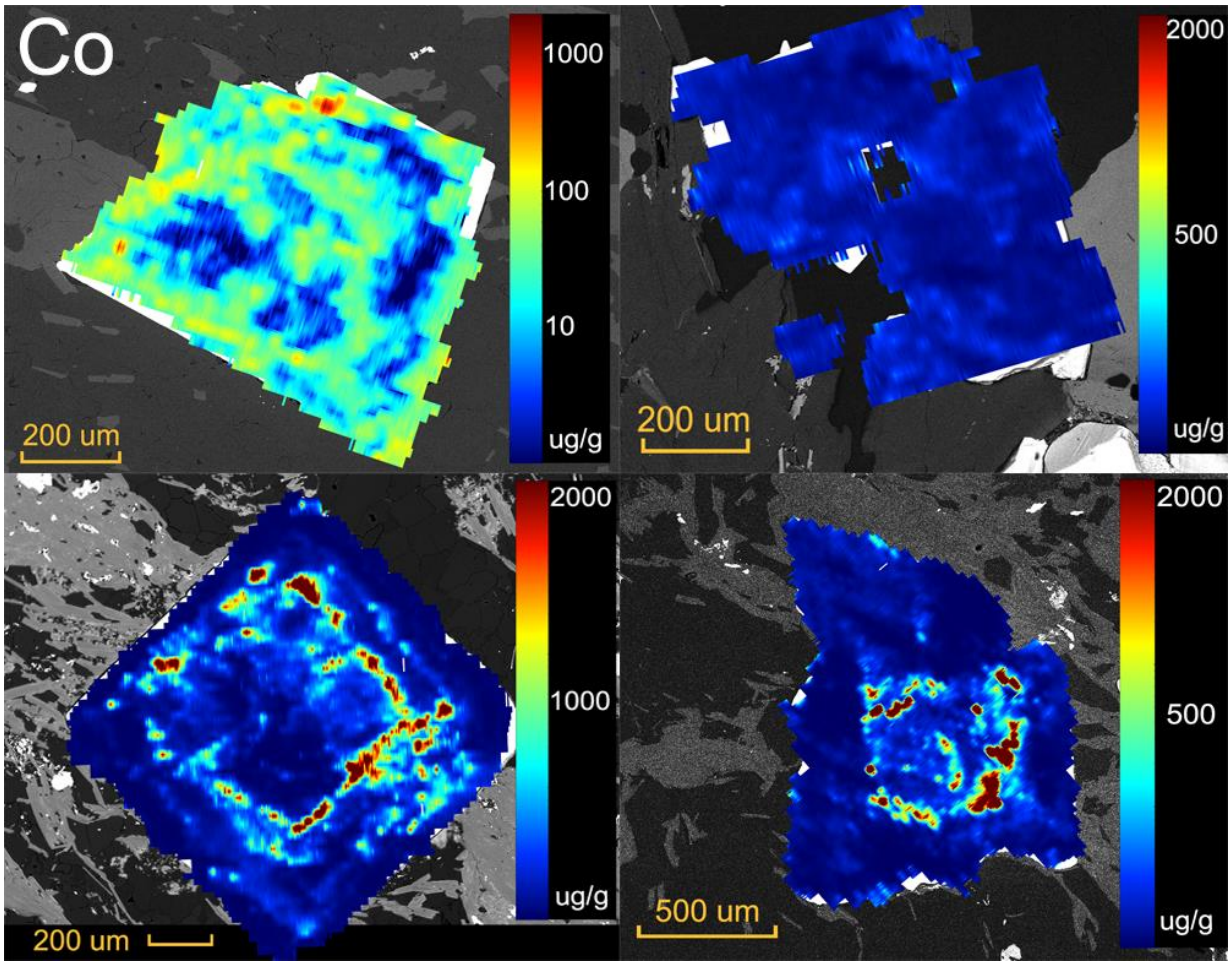

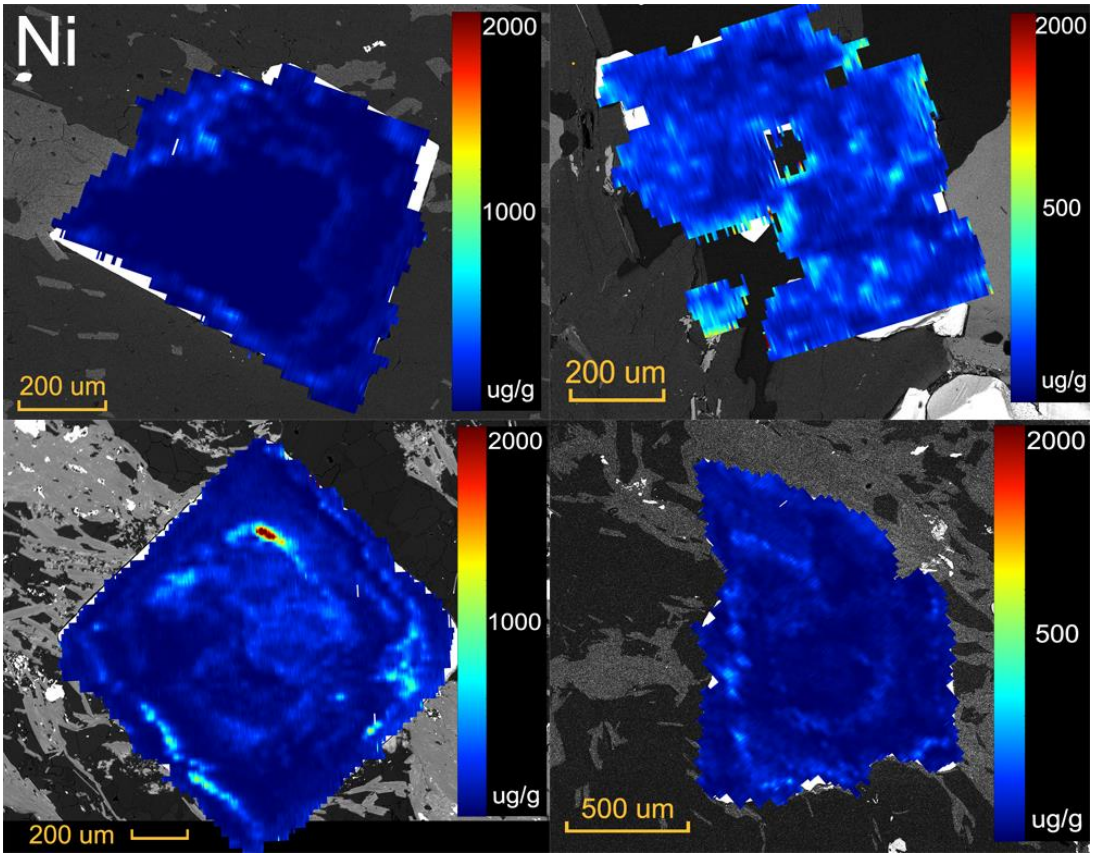
Ni
2000
1000
ug/g
200 um
2000
500
ug/g
200 um
2000
1000
ug/g
200 um
2000
500
ug/g
500 um

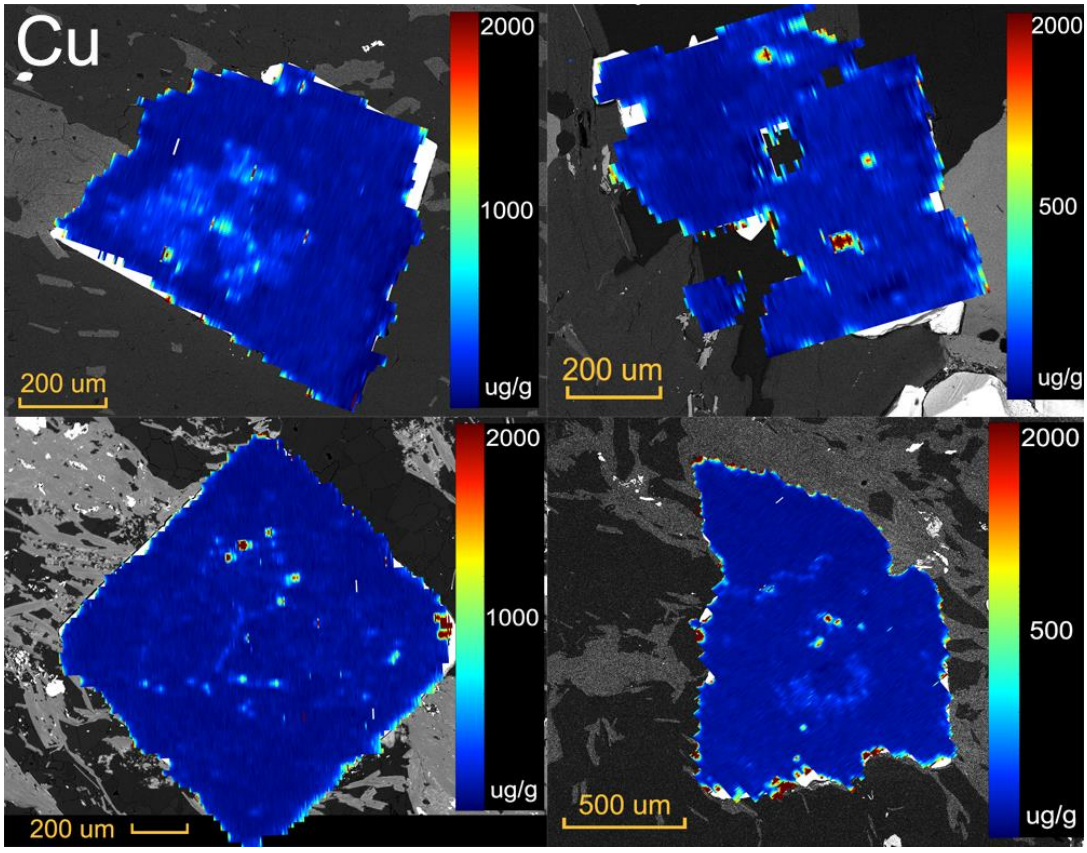
Cu
2000
1000
ug/g
200 um
2000
500
ug/g
200 um
2000
1000
ug/g
200 um
2000
500
ug/g
500 um

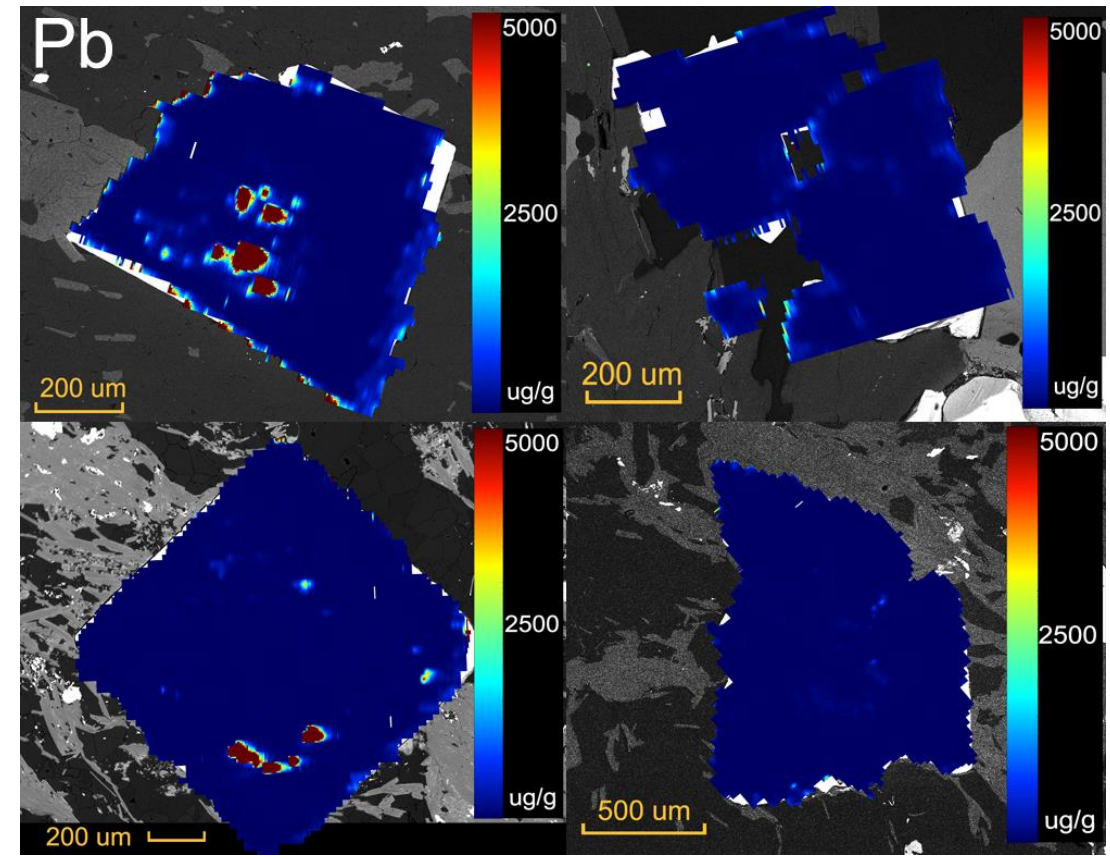
Pb
5000
2500
ug/g
200 um
5000
2500
ug/g
200 um
5000
2500
ug/g
200 um
5000
2500
ug/g
500 um

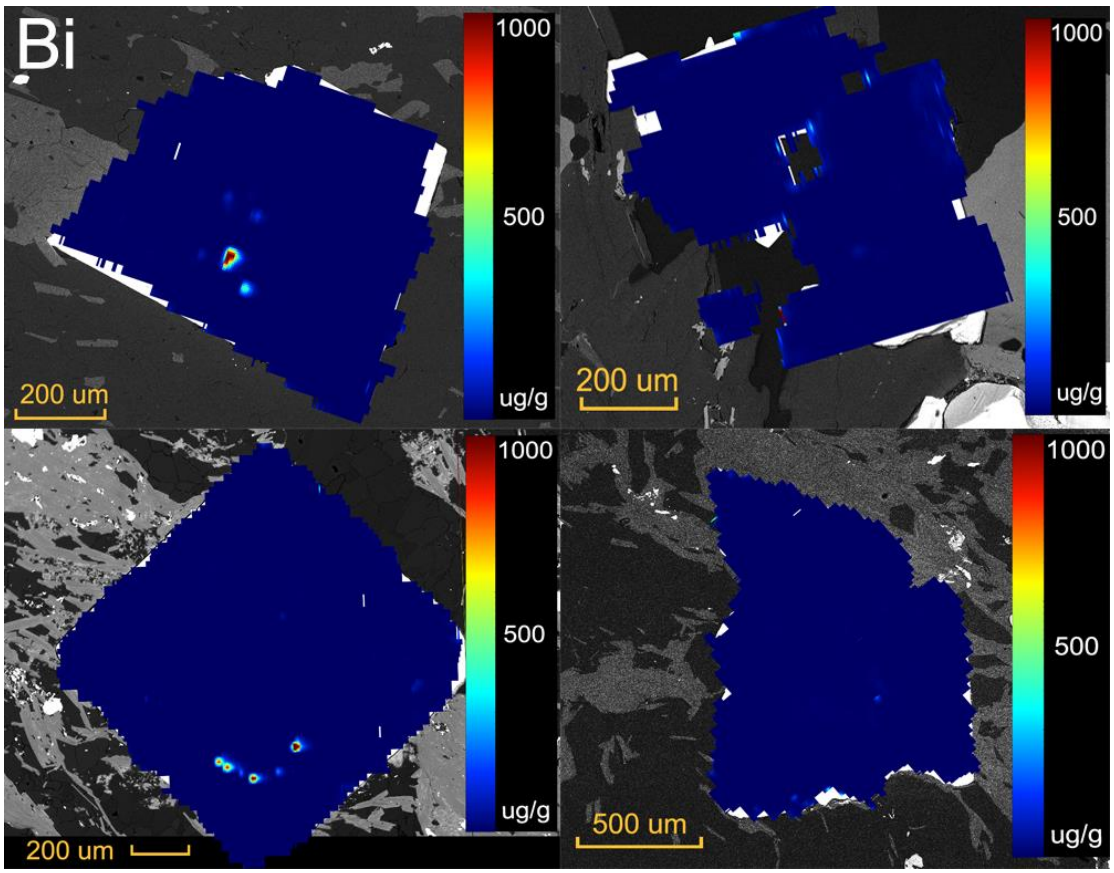
Bi
1000
500
ug/g
200 um
1000
500
ug/g
200 um
1000
500
ug/g
200 um
1000
500
ug/g
500 um

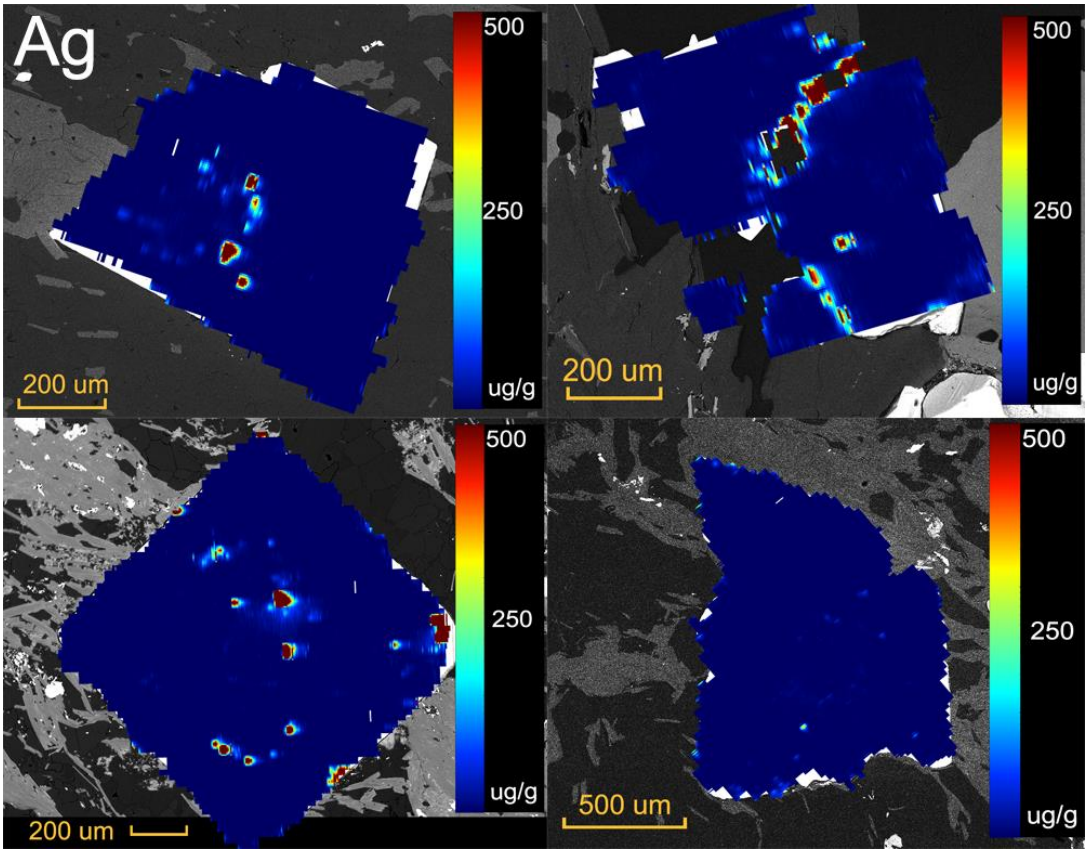
Ag
500
250
ug/g
200 um
500
250
ug/g
200 um
500
250
ug/g
200 um
500
250
ug/g
500 um

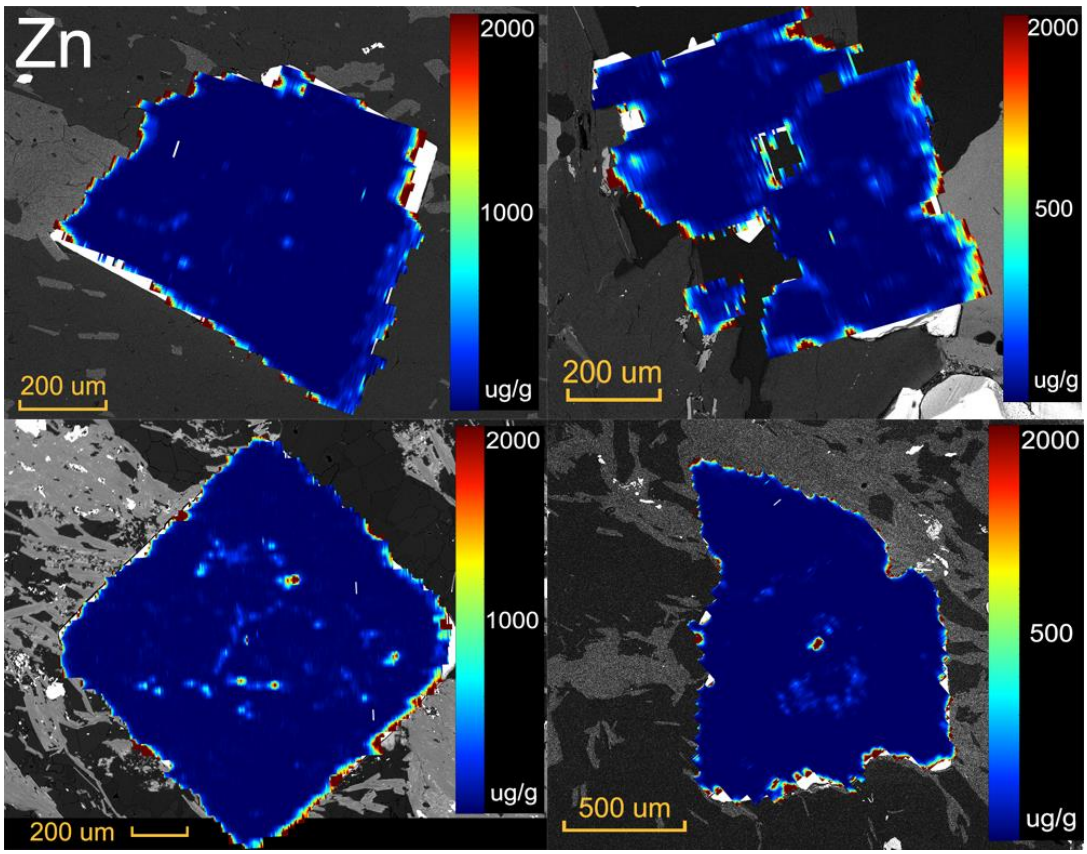
Zn
2000
1000
ug/g
200 um
2000
500
ug/g
200 um
2000
1000
ug/g
200 um
2000
500
ug/g
500 um

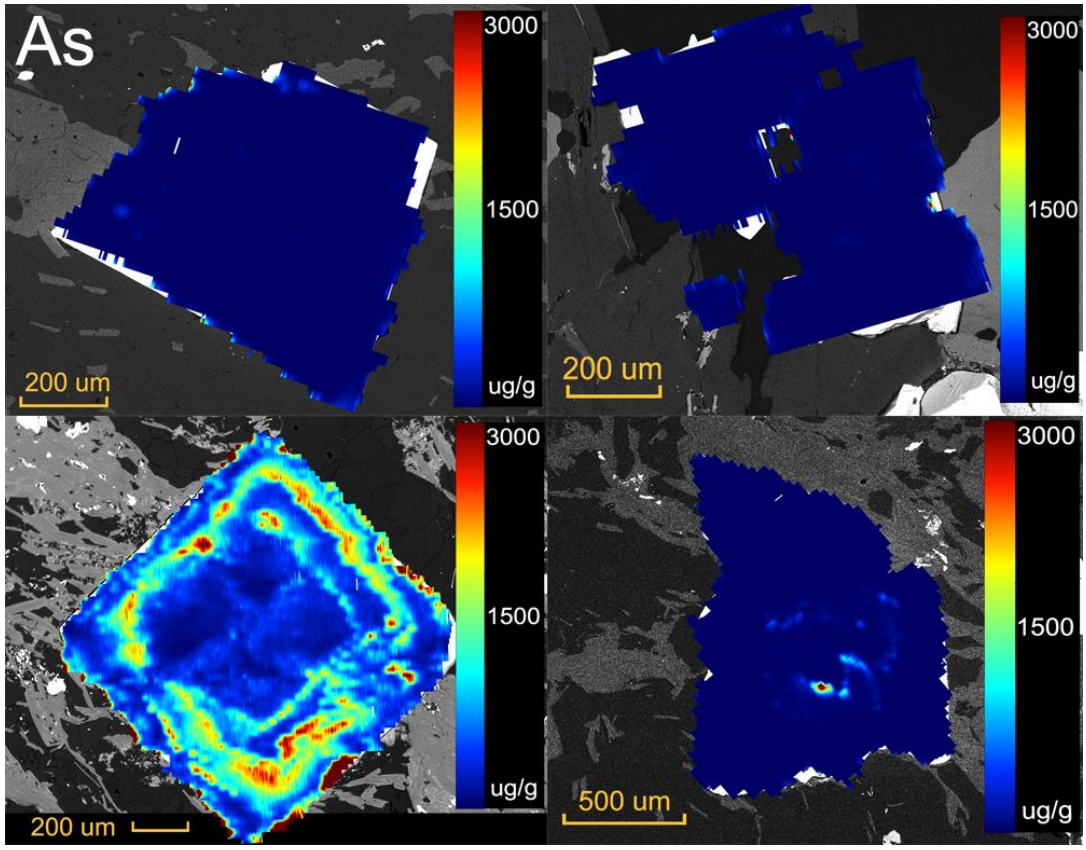
As
3000
1500
ug/g
200 um
3000
1500
ug/g
200 um
3000
1500
ug/g
200 um
3000
1500
ug/g
500 um

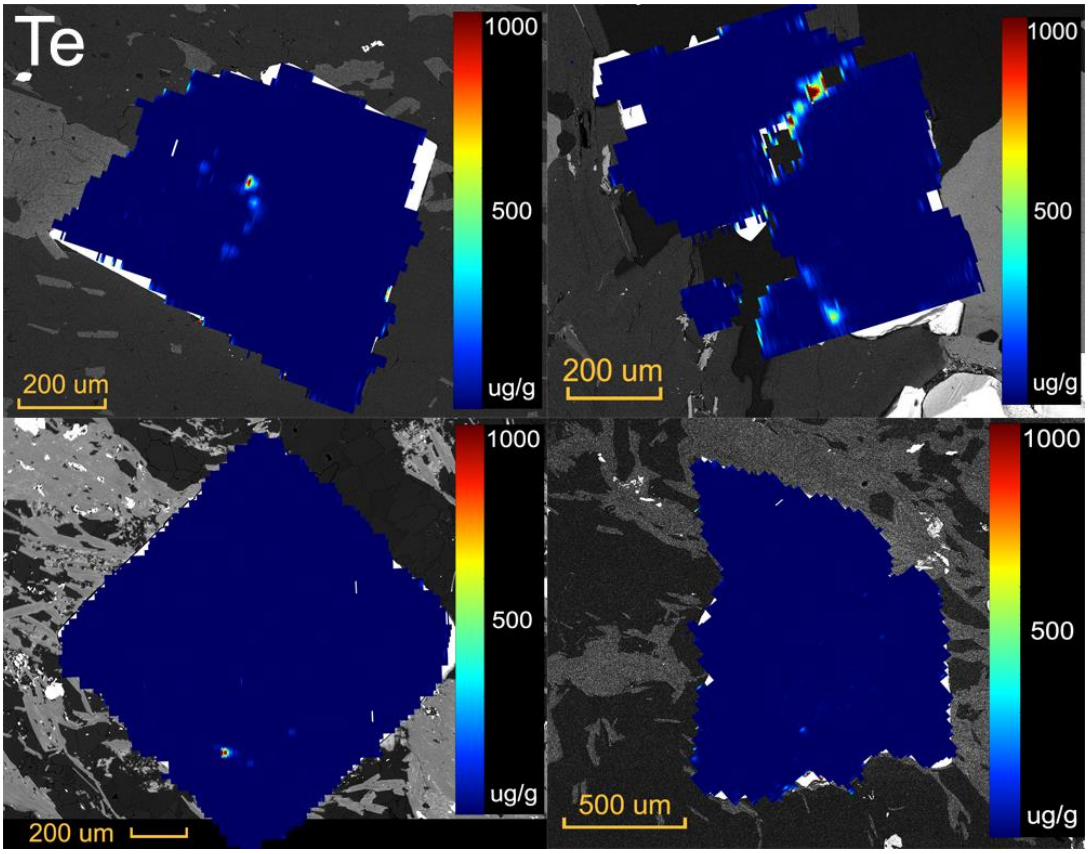
Te
1000
500
ug/g
200 um
1000
500
ug/g
200 um
1000
500
ug/g
200 um
1000
500
ug/g
500 um

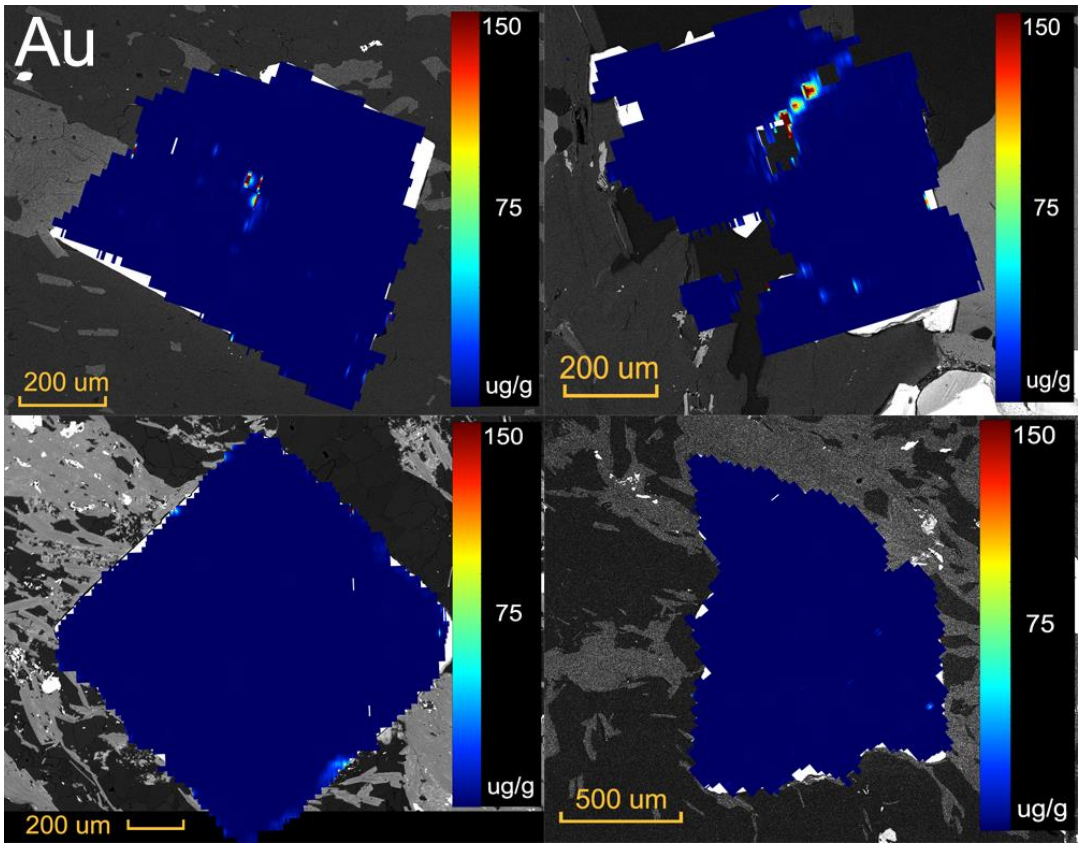
Au
150
75
ug/g
200 um
150
75
ug/g
200 um
150
75
ug/g
200 um
150
75
ug/g
500 um

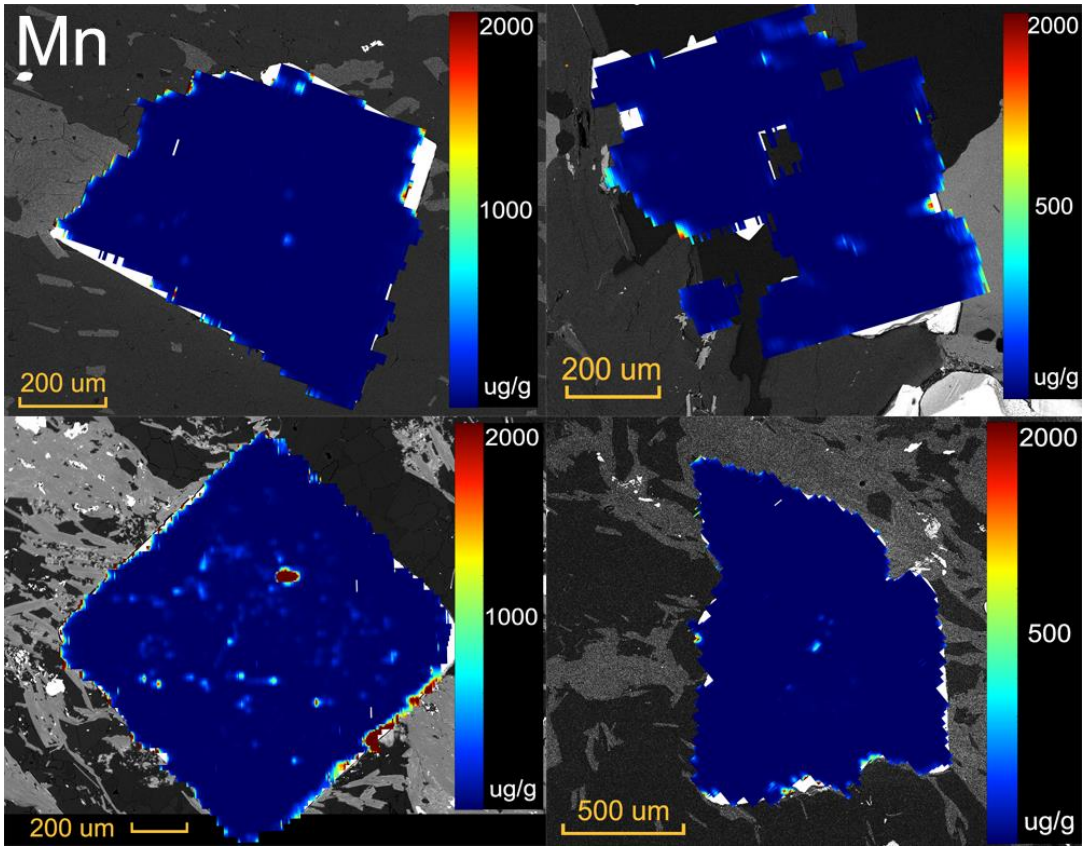
Mn
2000
1000
ug/g
200 um
2000
500
ug/g
200 um
2000
1000
ug/g
200 um
2000
500
ug/g
500 um

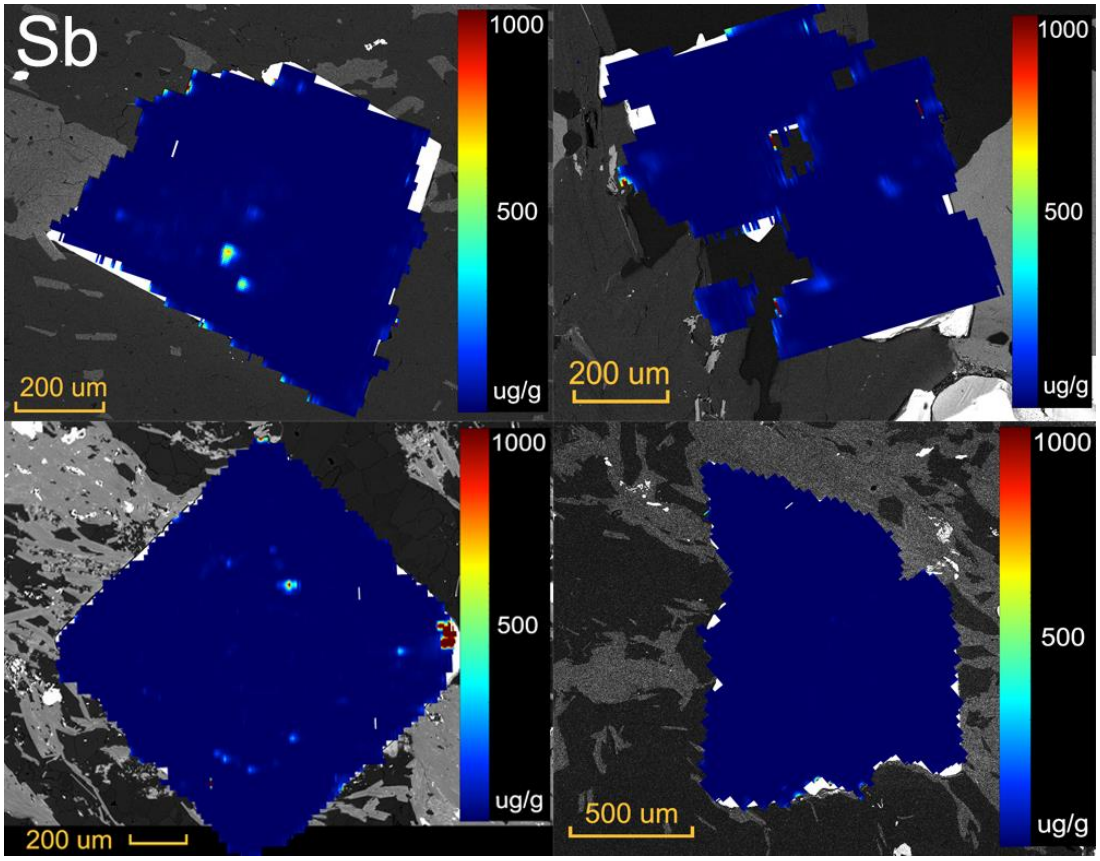
Sb
1000
500
ug/g
200 um
1000
500
ug/g
200 um
1000
500
ug/g
200 um
1000
500
ug/g
500 um

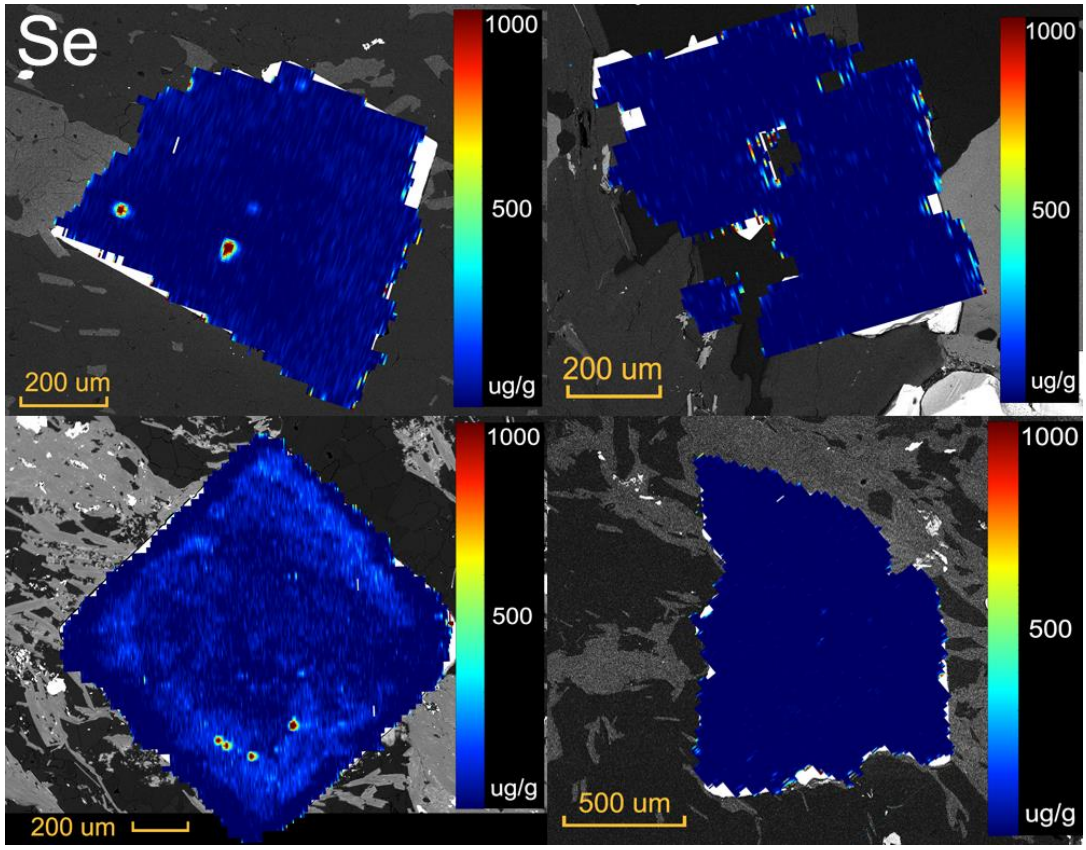
Se
1000
500
ug/g
200 um
1000
500
ug/g
200 um
1000
500
ug/g
200 um
1000
500
ug/g
500 um

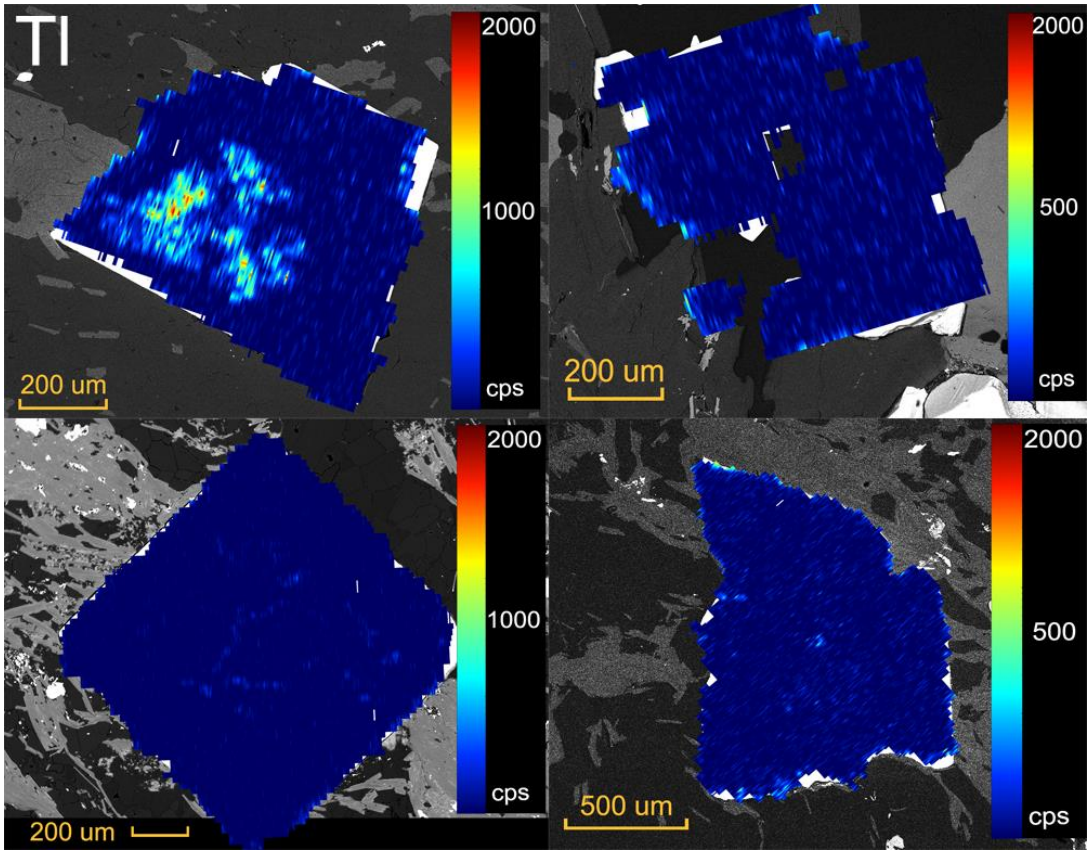
Tl
2000
1000
cps
200 um
2000
500
cps
200 um
2000
1000
cps
200 um
2000
500
cps
500 um

Appendix B: Petrographic Descriptions

LS17-91 Petrographic Report

Main matrix minerals:

Phengite

Quartz

Albite

Chlorite*

Secondary minerals:

Apatite

Rutile

Titanite

Zircon

Monazite

Hyalophane

Carbonate*

Sulfide Description:

Finer-grained Py than other samples, often sub-mm-scale, with highest overall proportion (Table 1). Pyrites tend to form small aggregates, inclusions reflect matrix mineralogy. Some grains appear elongate to local fabric, indicative of Py1 texture. Small galena and chalcopyrite inclusions are also noted. Native Au +/- Ag found along grain margins or in fractures of some grains

Dominant Structures:

Pervasive S2 foliation throughout hole, variable but relatively light S3 crenulation overprint. Occasional D4 structures usually expressed as kink-banding, hosting x-cutting quartz veins

Hole Description:

QMS (intermediate schist) phasing into MQ (felsic schist) member by 84m. Commonly observed carbonate and chlorite porphyroblast's overprinting main mineral assemblage. Throughout, quartz-mica proportions vary as to which is the dominant phase. Some zones contain highly chaotic deformation textures. Discordant quartz veins as well as metamorphic quartz segregations are common throughout.

General Comments:

- *Chlorite and carbonate not observed in EDS but noted as overprinting textures in field descriptions. Presence of Ca-carbonate verified during sampling with HCl.
- Interval contained a cross-cutting quartz vein that revealed visible gold during preparation, but wasn't polished due to general lack of pyrite in the vein
- Some monazites show evidence of REE incorporation (La, Nd)

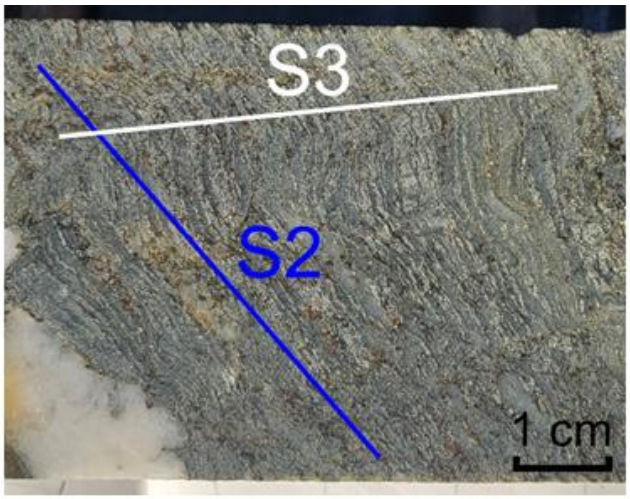

Image of field sample pre-preparation with labeled fabric

RFL photo of pyrite aggregates

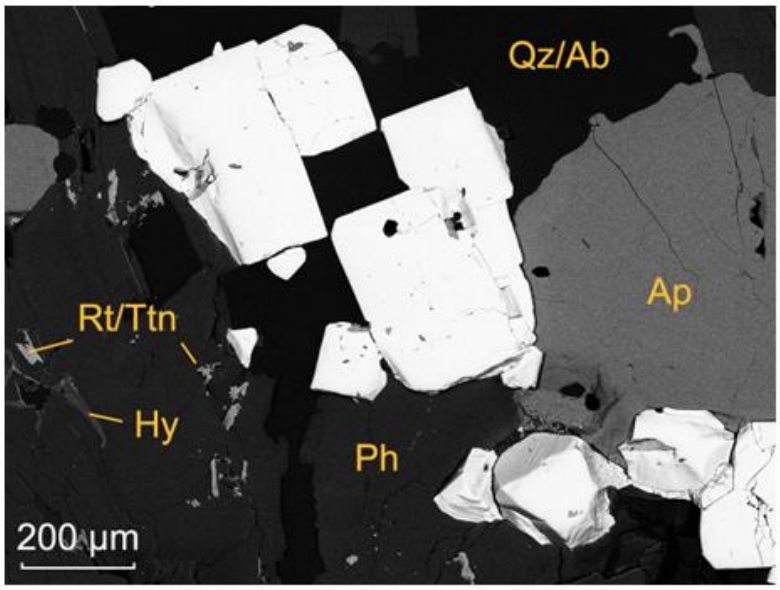

Labeled SEM photo close up of previous region

EC19-259 Petrographic Report

Main matrix minerals:

Phengite

Quartz

Albite

Chlorite*

Secondary minerals:

Apatite

Rutile

Titanite

Zircon

Monazite

Carbonate

Suflide Description:

Most coarse grained pyrites of all samples, grains occasionally reach 0.5 cm in areas. Almost entirely Py2 grains observed. Variable pyrite content, usually increases around veins up to few %. Inclusions of chalcopyrite, galena, and sphalerite observed

Dominant Structures:

Pervasive S2 foliation throughout hole, S3 expression as occasional light crenulation. D4 structures present occasionally, host x-cutting quartz veins

Hole Description:

Interpreted to be QMS (intermediate schist) throughout, this hole varies in silica content reducing given mica proportions in different regions. Usually muscovite becomes more dominant than chlorite in regions of higher SiO_2. Discordant quartz veins as well as metamorphic quartz segregations are common throughout.

General Comments:

- *Chlorite not observed in EDS but noted in field descriptions
- Selected interval was downhole from 2 discordant quartz veins, both with associated sulfidation and one bearing visible gold
- Some monazites show evidence of REE incorporation (La, Nd)

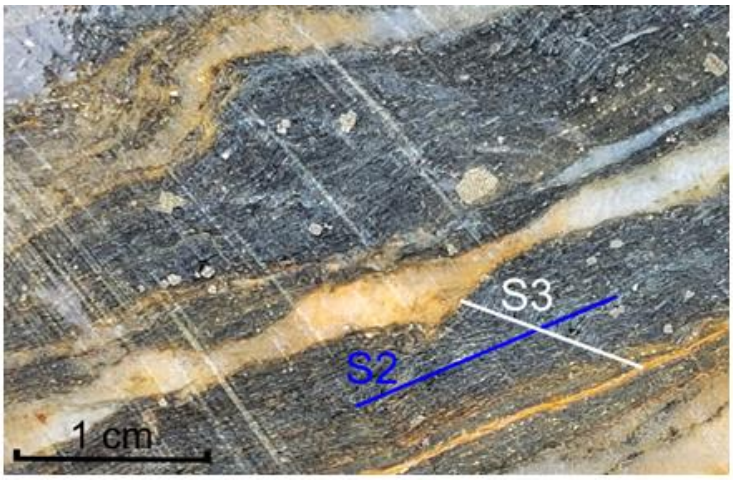

Image of field sample pre-preparation with labeled fabric

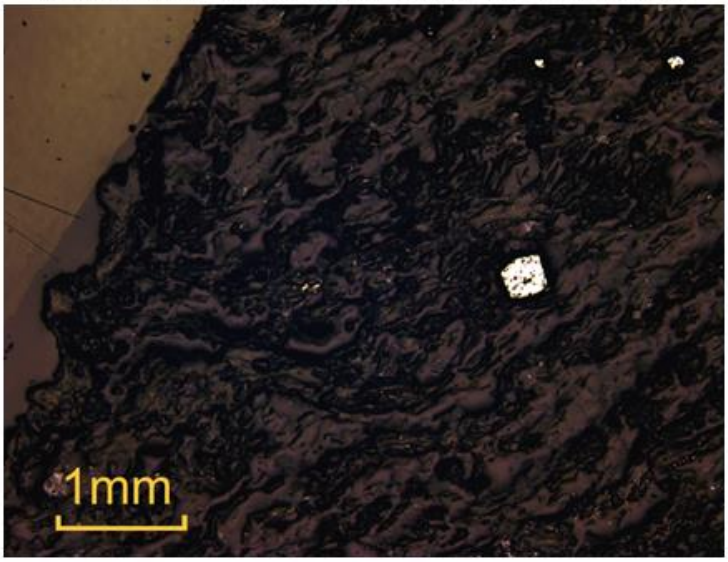

RFL photo of py2 occurence

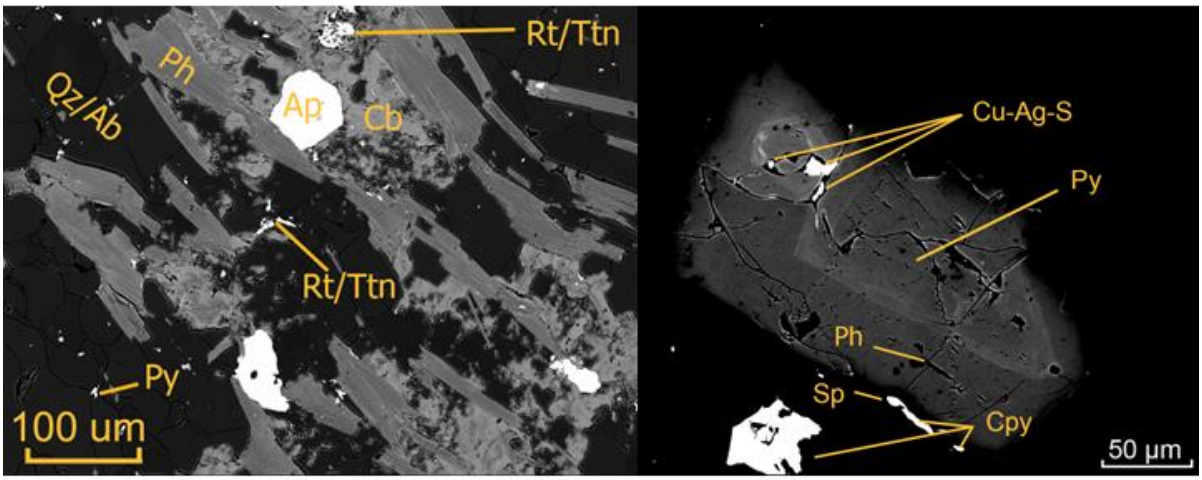

Labeled SEM photo of matrix as well as a grain of interest

EC19-333 Petrographic Report

Main matrix minerals:

Phengite
Quartz
Albite
Chlorite*

Suflide Description:

Py1 and Py2 both occur in this sample, grains averaged 0.5-1mm with examples up to ~5mm. Variable pyrite content, usually increases around veins up to few %. Inclusions of chalcopyrite commonly observed

Secondary minerals:

Apatite
Rutile
Zircon
Monazite
Carbonate*
Barite
Scheelite

Dominant Structures:

Pervasive S2 foliation throughout hole, fabric occasionally becoming ptygmatic or chaotic. In our section, S2 is present deformed by spaced D3 crenulations. D4 structures present occasionally, host x-cutting quartz veins

Hole Description:

Interpreted as QMS, (intermediate schist), and similar to other samples, variable in silica content which affects mica proportions: phengite dominates when SiO_2 increases. Discordant quartz veins as well as metamorphic quartz segregations are common throughout.

General Comments:

- *Chlorite not observed in EDS but noted in field descriptions
- Phengite in this sample ranges in K and Mg significantly
- Some monazites show evidence of REE incorporation (La, Nd)
- Albite seems particularly abundant in this section

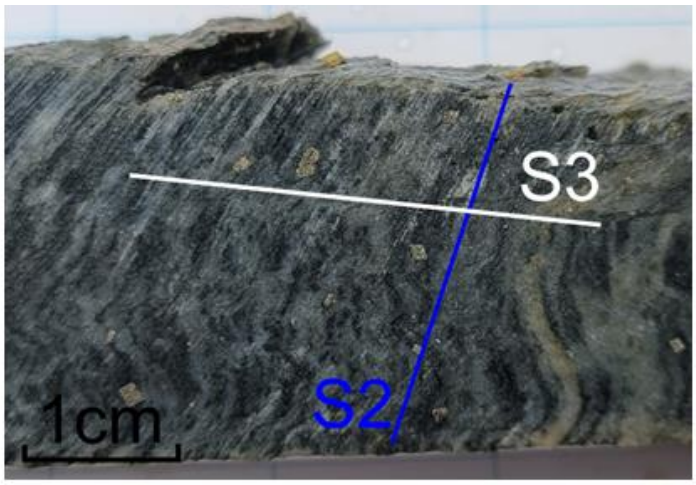

Image of field sample pre-preparation with labeled fabric

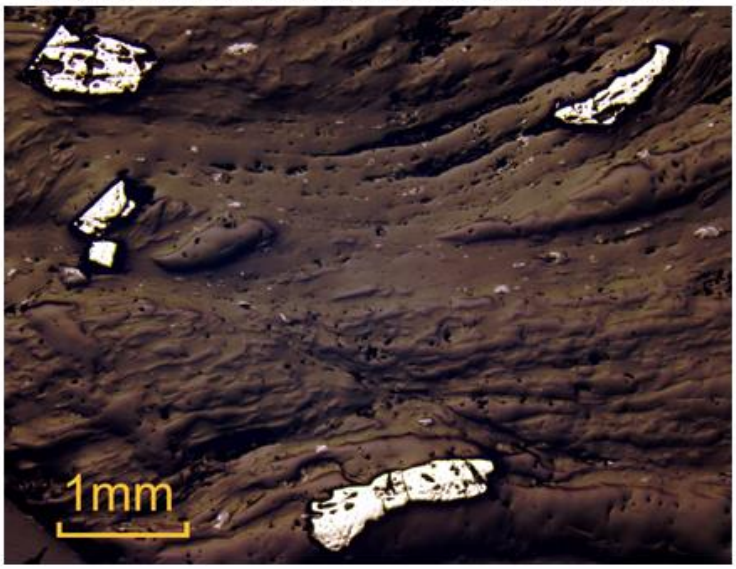

RFL photo of py occurrences

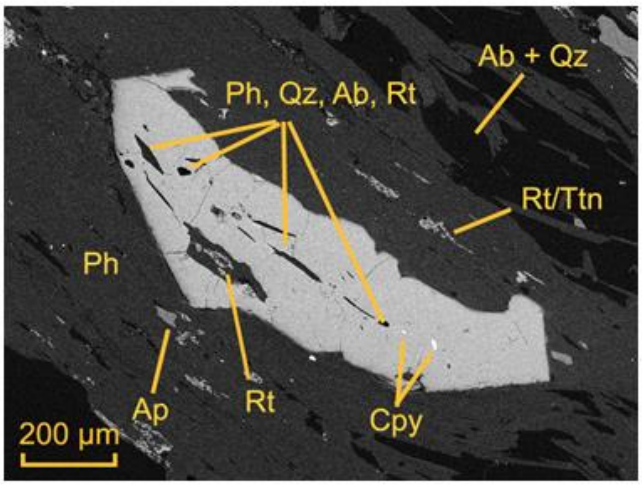

Labeled SEM photo of a grain of interest

EC22-481 Petrographic Report

Primary vein minerals:

Ankerite

Quartz

Secondary vein minerals:

Barite

Rutile

Flourite

Primary matrix minerals:

Phengite

Quartz

Albite

Chlorite*

Secondary matrix minerals:

Apatite

Rutile

Scheelite

Suflide Description:

This is the only Py3 sample analyzed, with a Py2 grain in a piece of matrix on the edge. Pyrite proportion in the vein visually estimated at 1%. Average sized grains, on typically on the mm-scale.

Vein description:

Sample was received as a cutting fragment, as such full descriptions of this sample in its specific context were not performed. Vein contacts are scalloped, obscuring the structure that hosts it. SEM imaging reveals reaction textures between quartz and carbonate at contacts, and these regions typically have the highest proportion of accessory minerals, in particular barite and fluorite. Very fine grained disseminated pyrite is found in these sections as well.

Hole Description:

Interpreted as QMS, (intermediate schist) throughout hole. Lithologic descriptions are not complete for this unit, but generally similar to other holes regarding discordant veins, quartz/mica proportions and structural trends.

General Comments:

- *Chlorite not observed in EDS but noted in field descriptions
- Native Au identified in quartz veins uphole from this sample

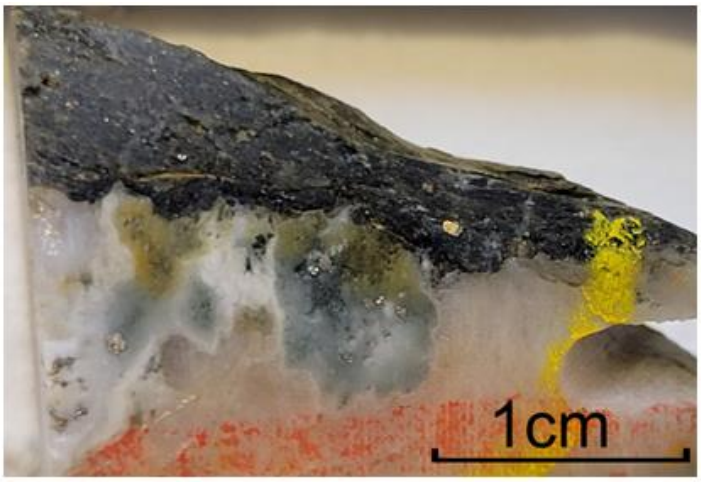

Image of field sample pre-preparation with labeled fabric

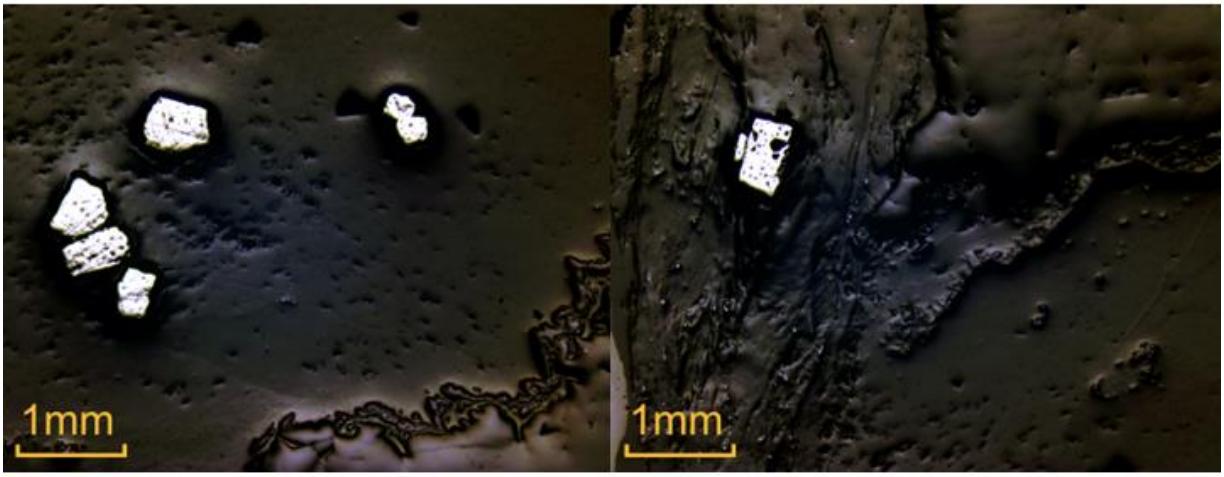

RFL photos of py occurrences

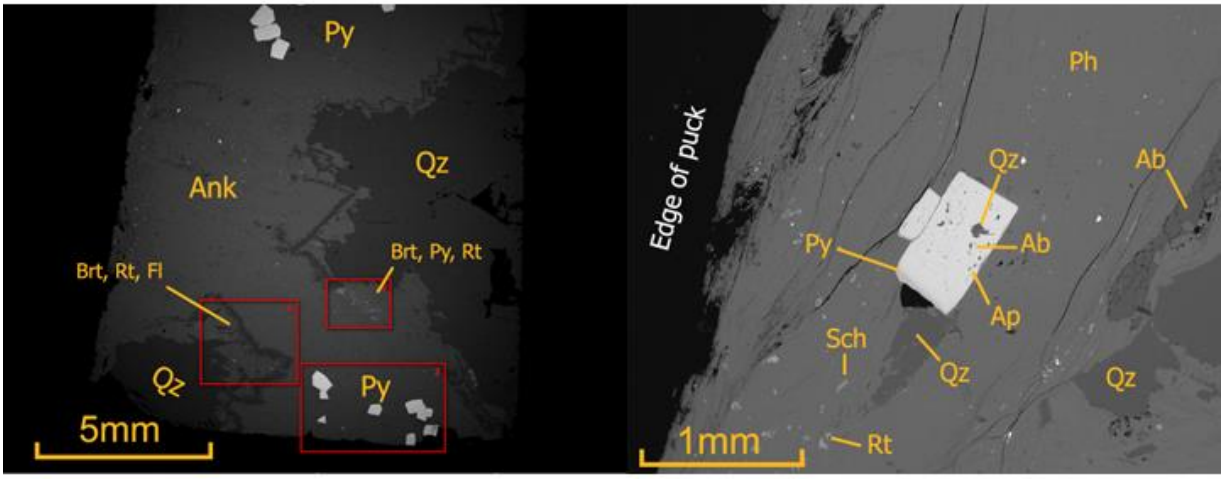

Labeled SEM photos of Py occurences

LS19-287A/B Petrographic Report

Main matrix minerals:

Phengite

Quartz

Albite

Chlorite*

Secondary minerals:

Apatite

Rutile

Titanite

Zircon

Monazite

Carbonate*

Barite

Scheelite

Suflide Description:

Py1 and Py2 both occur in this sample, with most proportion of Py1 of any sample. Grains averaged on the 0.5 mm-scale but ranged up to a few mm. Pyrite content varies from trace up to 3% across hole but is generally pyritic. Chalcopyrite commonly observed in trace proportions. Native Au + Ag found along a grain margin.

Dominant Structures:

Pervasive S2 foliation throughout hole, with S3 often overprinting and fabric at times becoming chaotic. Our sample contains a pervasive S2 foliation with a spaced S3 crenulation overprint.

Hole Description:

Interpreted as QMS, (intermediate schist), and similar to other samples, variable in silica content which affects mica proportions: phengite dominates when SiO_2 increases. Discordant quartz veins as well as metamorphic quartz segregations are common throughout. Overprinting chlorite and carbonate porphyroblasts noted throughout hole

General Comments:

- *Chlorite not observed in EDS but noted in field descriptions

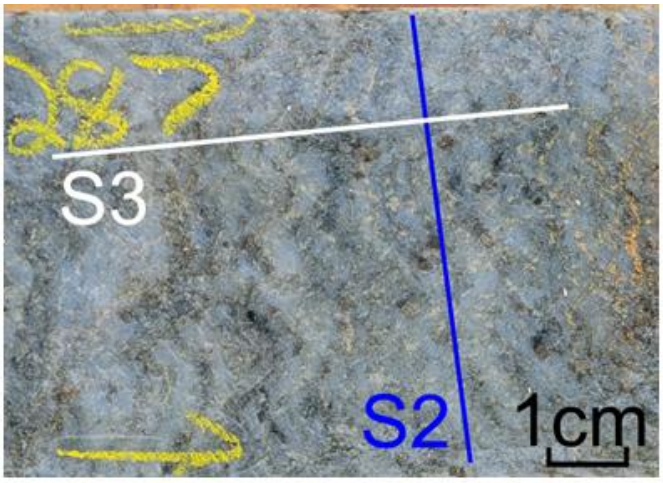

Image of field sample pre-preparation with labeled fabric

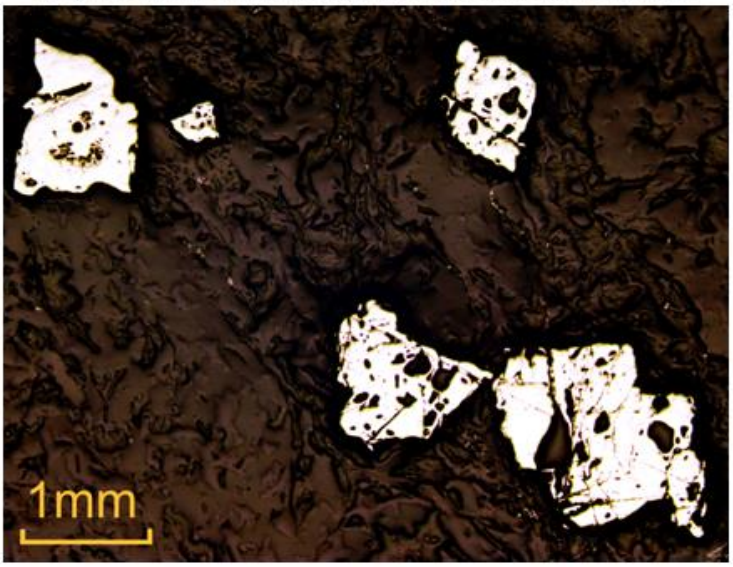

RFL photo of py occurrences

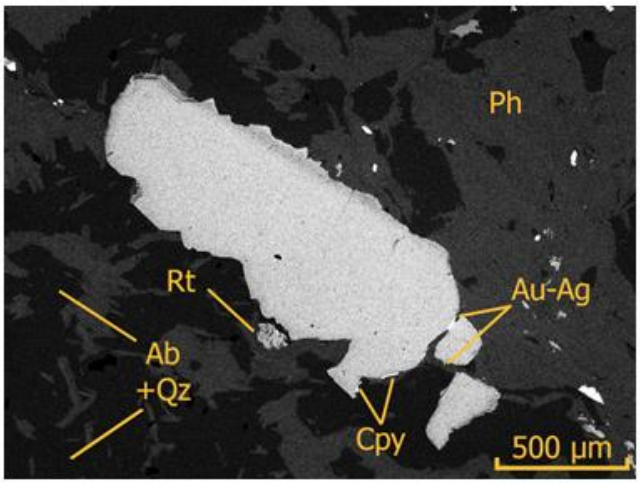

Labeled SEM photo of a grain of interest

LS20-379 Petrographic Report

Main matrix minerals:

Phengite

Quartz

Albite

Chlorite*

Secondary minerals:

Apatite

Rutile

Titanite

Zircon

Monazite

Barite

Suflide Description:

Pyrite occurs at mostly trace abundance in this section, almost exclusively as Py2, with only one possible Py1 grain identified. Grains are on mm-scale, with some finer grained disseminated pyrite noted. Galena, chalcopyrite, and sphalerite inclusions are all commonly documented in this zone.

Dominant Structures:

Pervasive S2 foliation throughout hole, with S3 often overprinting and fabric at times becoming chaotic. Our sample records S2 fabric almost exclusively. This unit is known for this feature, which is nearly diagnostic for it.

Hole Description:

QMS (intermediate schist) contacting MQ (felsic schist) at approx. 50.1m. Sample taken within MQ. Schist composition remains relatively constant in this unit, with common foliation-parallel quartz segregations. Hosts rarer discordant veins on average, possibly due to the relatively higher competency than other units. Also displays occasional small overprinting feldspar phenocrysts, which is not uncommon for this unit.

General Comments:

- *Chlorite not observed in EDS but noted in field descriptions
- Barite is in it's highest proportion in this sample
- Barite occasionally incorporates Co
- Sample generally lacked carbonate in matrix

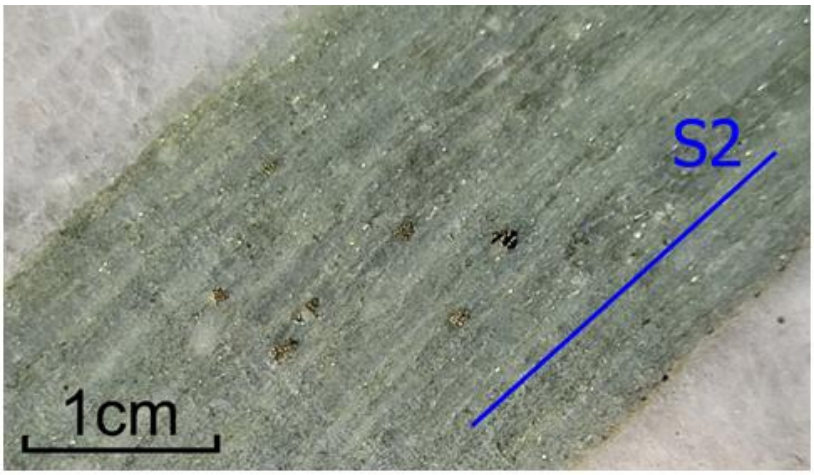

Image of field sample pre-preparation with labeled fabric

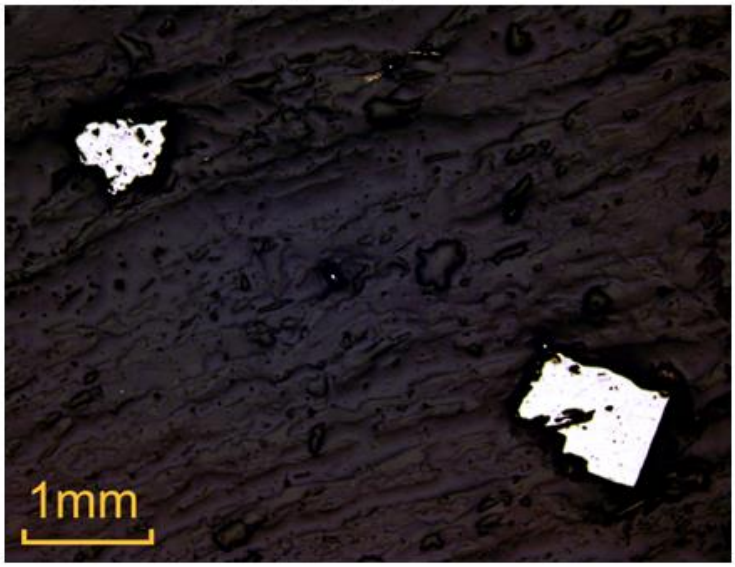

RFL photo of Py occurrences

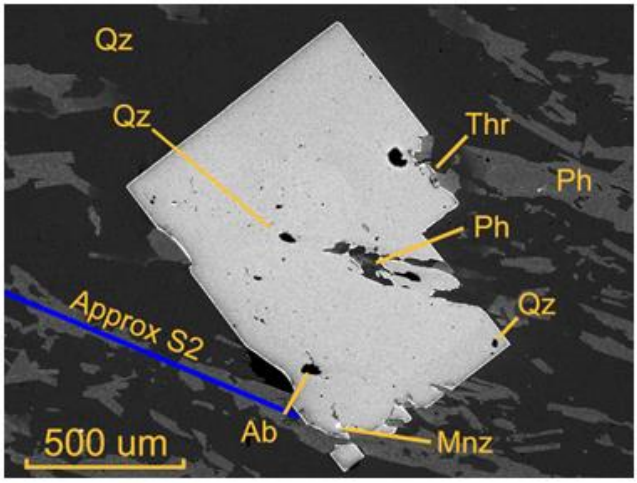

Labeled SEM photo of a grain of interest